ARMY RESEARCH LABORATORY

ARL

Control of Defects in Aluminum Gallium Nitride ((Al)GaN) Films on Grown Aluminum Nitride (AlN) Substrates

by Iskander G. Batyrev, Chi-Chin Wu, Peter W. Chung, N. Scott Weingarten and Kenneth A. Jones

ARL-TR-6350 February 2013

Approved for public release; distribution unlimited.

NOTICES

Disclaimers

The findings in this report are not to be construed as an official Department of the Army position unless so designated by other authorized documents.

Citation of manufacturer’s or trade names does not constitute an official endorsement or approval of the use thereof.

Destroy this report when it is no longer needed. Do not return it to the originator.

Army Research Laboratory
Aberdeen Proving Ground, MD 21005-5069

ARL-TR-6350 **February 2013**

Control of Defects in Aluminum Gallium Nitride ((Al)GaN) Films on Grown Aluminum Nitride (AlN) Substrates

Iskander G. Batyrev and N. Scott Weingarten
Weapons and Materials Research Directorate, ARL

Chi-Chin Wu and Peter W. Chung
Computational and Information Sciences Directorate, ARL

Kenneth A. Jones
Sensors and Electron Devices Directorate, ARL

Approved for public release; distribution unlimited.

REPORT DOCUMENTATION PAGE

Form Approved
OMB No. 0704-0188

Public reporting burden for this collection of information is estimated to average 1 hour per response, including the time for reviewing instructions, searching existing data sources, gathering and maintaining the data needed, and completing and reviewing the collection information. Send comments regarding this burden estimate or any other aspect of this collection of information, including suggestions for reducing the burden, to Department of Defense, Washington Headquarters Services, Directorate for Information Operations and Reports (0704-0188), 1215 Jefferson Davis Highway, Suite 1204, Arlington, VA 22202-4302. Respondents should be aware that notwithstanding any other provision of law, no person shall be subject to any penalty for failing to comply with a collection of information if it does not display a currently valid OMB control number.
PLEASE DO NOT RETURN YOUR FORM TO THE ABOVE ADDRESS.

<table>
<tr><td>1. REPORT DATE (DD-MM-YYYY)
February 2013</td><td>2. REPORT TYPE
DRI</td><td>3. DATES COVERED (From - To)
FY12</td></tr>
<tr><td colspan="2">4. TITLE AND SUBTITLE
Control of Defects in Aluminum Gallium Nitride ((Al)GaN) Films on Grown Aluminum Nitride (AlN) Substrates</td><td>5a. CONTRACT NUMBER

5b. GRANT NUMBER

5c. PROGRAM ELEMENT NUMBER</td></tr>
<tr><td colspan="2">6. AUTHOR(S)
Iskander G. Batyrev, Chi-Chin Wu, Peter W. Chung, N. Scott Weingarten and Kenneth A. Jones</td><td>5d. PROJECT NUMBER
FY12-WMR-048
5e. TASK NUMBER

5f. WORK UNIT NUMBER</td></tr>
<tr><td colspan="2">7. PERFORMING ORGANIZATION NAME(S) AND ADDRESS(ES)
U.S. Army Research Laboratory
ATTN: RDRL WMB-B
4600 Deercreek Loop
Aberdeen Proving Ground, MD 21005-5069</td><td>8. PERFORMING ORGANIZATION REPORT NUMBER
ARL-TR-6350</td></tr>
<tr><td colspan="2">9. SPONSORING/MONITORING AGENCY NAME(S) AND ADDRESS(ES)</td><td>10. SPONSOR/MONITOR'S ACRONYM(S)

11. SPONSOR/MONITOR'S REPORT NUMBER(S)</td></tr>
<tr><td colspan="3">12. DISTRIBUTION/AVAILABILITY STATEMENT
Approved for public release; distribution unlimited.</td></tr>
<tr><td colspan="3">13. SUPPLEMENTARY NOTES</td></tr>
</table>

14. ABSTRACT

We present efforts aimed at establishing a multiscale approach for simulating dislocations in aluminum gallium nitride ((Al)GaN) semiconductors. We performed quantum mechanical and classical molecular dynamics (MD) simulations to study the electronic and atomic structure of threading edge and screw dislocations in AlGaN, focusing on the structure of the dislocation core and the electrical activity of dislocations, and estimating dislocation velocities as a function of applied stress and temperature. We used the calculated mobility functions from MD to study different junction configurations using a discrete dislocation dynamics (DDD) simulator, ParaDiS. Finally, we predicted the most likely slip planes in wurtzite (Al)GaN semiconductors based on general crystallographic principles. The most important results are (1) aluminum (Al) atoms do not segregate to the dislocation core and atoms in the dislocation core do not produce any defect levels in the bandgap; (2) we performed first time classical MD calculations of dislocation velocity as a function of applied stress for three slip systems in gallium nitride (GaN); (3) we adapted ParaDiS to simulate wurtzite semiconductors; and (4) the plane strain produced by the lattice mismatch during growth on the $(\mathbf{0001})$ plane does not create a shear stress on the basal or prismatic planes, hence the operational slip plane must be a pyramidal plane, the most probable being the $\frac{1}{3}\langle\mathbf{11\bar{2}\bar{3}}\rangle\{\mathbf{11\bar{2}2}\}$ slip system.

15. SUBJECT TERMS

Dislocations, modeling, semiconductors, Director's Research Initiative (DRI)

<table>
<tr><td colspan="3">16. SECURITY CLASSIFICATION OF:</td><td rowspan="2">17. LIMITATION OF ABSTRACT
UU</td><td rowspan="2">18. NUMBER OF PAGES
46</td><td>19a. NAME OF RESPONSIBLE PERSON
Iskander G. Batyrev</td></tr>
<tr><td>a. REPORT
Unclassified</td><td>b. ABSTRACT
Unclassified</td><td>c. THIS PAGE
Unclassified</td><td>19b. TELEPHONE NUMBER (Include area code)
(410) 306-4582</td></tr>
</table>

Standard Form 298 (Rev. 8/98)
Prescribed by ANSI Std. Z39.18

Contents

List of Figures iv

List of Tables vi

1. Objectives 1

2. Introduction 1

3. Description of the Dislocations 3

4. Classical Molecular Dynamics Simulations of Dislocations in GaN 6

5. Non-coplanar Binary Dislocation Junctions in Hexagonal Close-packed Crystals 10

5.1 Approach 10

5.2 Formation of Equilibrium Junctions 13

5.3 Junction Unzipping and Yield Surfaces 13

5.4 The Effect of Dislocation Length on Critical Unzipping Stresses 16

5.5 Wurtzite GaN 17

6. Quantum Mechanical Simulations of Dislocations in AlGaN 18

7. Crystallographic Theory of Dislocations in GaN 19

7.1 Derivation of Most Probable Slip Systems 19

7.2 Discussion 29

8. Conclusions 30

9. References 32

10. Transitions 35

List of Symbols, Abbreviations, and Acronyms 36

Distribution List 38

List of Figures

Figure 1. The sp^3 bonding structure typical in most semiconductors. (a) The tetrahedron formed by the four cations that surround the anion inside of it. (b) Same, with ions not visualized. (c) A *cpp* and the B and C sites for the *cpp* that can lie above it. 3

Figure 2. (a) The sp^3 tetrahedron in the hexagonal W structure with its green base parallel to the 0002 *cpp*. (b) The stacking structure of W crystal. 4

Figure 3. (a) The cube used to construct the sp^3 tetrahedron in a ZB cubic unit cell and (b) the cubic ZB unit cell. 5

Figure 4. (a) The four equivalent $\{111\}$ type slip planes in the cubic ZB structure. (b) The $\left[\frac{1}{2}\ 0\ -\frac{1}{2}\right]$ Burgers vector and the $[01\bar{1}]$ dislocation line for the 60° dislocation line in the (111) plane of a cubic ZB structure. 6

Figure 5. Method of generating a dislocation in a single crystal: (a) two half planes are removed from the lower half and after equilibration, (b) a dislocation remains near the center of the system, a close-up of which is seen in (c). 7

Figure 6. A depiction of the simulation technique to measure dislocation velocity as a function of applied stress. 8

Figure 7. Example of dislocation glide. The visualization software is AtomEye (*8*). 8

Figure 8. Position of dislocation as a function of nominal time for three different values of applied stress. 9

Figure 9. Log-log plot of dislocation velocity as a function of applied stress for the three slip systems identified in the legend. 10

Figure 10. Illustration showing the selected different interacting slip systems: The purple arrows represent the Burgers vectors for the dislocation on the $(01\bar{1}0)$ plane (also in purple). The red arrows represent the Burgers vectors for the dislocation on the (0001) plane in case (a) and on the $(\bar{2}112)$ plane in cases (b) and (c), respectively. 11

Figure 11. The yield surfaces for case (a). σ_1' and σ_2' are the normalized resolved applied stresses on the (0001) and the $(01\bar{1}0)$ planes, respectively. The junction is oriented along $\left[1\ \sqrt{3}\ 0\right]$, equivalent to $[\bar{2}110]$ in the 4-index notation. 14

Figure 12. The yield surfaces for case (b). σ_1' and σ_2' are the normalized resolved applied stresses on the $(\bar{2}112)$ and the $(01\bar{1}0)$ planes, respectively. The junction is oriented along $\left[1\ -\sqrt{3}\ 0\right]$, equivalent to $[\bar{2}110]$ in the 4-index. notation. 14

Figure 13. The yield surfaces for case (c). σ_1' and σ_2' are the normalized resolved applied stresses on the $(\bar{2}112)$ nd the $(01\bar{1}0)$ planes, respectively. The junction is oriented along $\left[1\ -\sqrt{3}\ 0\right]$, equivalent to $[\bar{2}110]$ in the 4-index notation. 15

Figure 14. The yield surfaces for the junction in Be in case (a) with varying initial dislocation lengths, *L*. The junction is oriented along $[1-\sqrt{3}\;0]$, equivalent to $[\bar{2}110]$ in the 4-index notation. 17

Figure 15. Distribution of Al atoms in (a) screw and (b) edge dislocations in $Al_{0.25}Ga_{0.75}N$ after 10 generations of an evolution with 8 members in each generation. Total charge distribution at isovalue of 0.2 is also shown in the picture. Shadowed region corresponds to Brillouin zone of the supercell. 19

Figure 16. (a) Schematic of a dislocation loop and its associated Burgers vectors, dislocation lines, and partial dislocations for the ZB structure for hetero-epitaxial growth on the (111) plane. (b) The sp^3 tetrahedron for the ZB structure with the apex at the origin and the base of the inverted pyramid being parallel to the (111) plane. (c) Atomic packing of the close packed $(1\bar{1}\bar{1})$ ZB plane and the $\frac{1}{2}[\bar{1}0\bar{1}]$ Burgers vector with its associated 60° dislocation line and associated PDs. (d) Atomic packing of the close packed (111) ZB plane, the $\frac{1}{2}[10\bar{1}]$ Burgers vector, with its associated 60° dislocation line and associated PDs. 20

Figure 17. Schematic of the (a) $(01\bar{1}1)$, (b) $(11\bar{2}2)$, and (c) $(2\bar{1}\bar{1}1)$ W planes and the $\frac{1}{3}[11\bar{2}\bar{3}]$ dislocation and associated dislocation line lying in the interfacial (0001) plane. 22

Figure 18. (a) Top (111) planar view and ABA … stacking of the $(10\bar{1})$ ZB planes and the equivalent $(2\bar{1}\bar{1}0)$ W planes. (Cations in ○, ½ or ⅓ above △, and ⅔ above □ the plane; anions ⅜ or ¼ above ●, ⅞ or ½ above ▲, and ¾ above ■.) (b) Side $(2\bar{1}\bar{1}0)$ planar view of the W structure showing the AαBβAα... stacking of the (0002) planes, and (c) side equivalent $(10\bar{1})$ planar view of the ZB structure showing the AαBβCγAα... stacking of the (111) planes. (Cations ○ and anions ● in, cations △ or △, and anions ▲ or ▲ ½ in front of, and cations □ or □ and anions □ or □ ½ behind the plane.) 23

Figure 19. (a) Top (0002) planar view and ABCDA … stacking of the $(1\bar{1}00)$ W planes. (b) Side $(1\bar{1}00)$ planar view of the W structure showing the AαBβAα... stacking of the (0002) planes. (c) Top (111) planar view and ABCDEF … stacking of the $(2\bar{1}\bar{1})$ ZB planes. (d) Side $(2\bar{1}\bar{1})$ planar view of the ZB structure showing the AαBβCγAα... stacking of the (111) planes. (Cation ○ and anion ● in, cation ⬡ and anion ⬢ $^1/_6$ behind, cation △ and anion ▲ ⅓ behind, cation ◇ and anion ◆ ½ behind, cation ⬠ and anion ⬟ ⅔ behind, and cation □ and anion ■ $^5/_6$ behind the plane.) 24

Figure 20. View of the Ga atoms lying in ○, immediately above △, and immediately below □, and the N atoms lying immediately above ▲ and immediately below ■ the (a) $(11\bar{2}2)$ W plane, or (b) $(13\bar{1})$ ZB plane. 28

List of Tables

Table 1. Slip planes and Burgers vectors. 11
Table 2. The Burgers vectors and directions of the resultant binary junctions. 12
Table 3. Properties of the equilibrium junctions. 13
Table 4. A description of the $\frac{1}{3}[11\bar{2}\bar{3}]$ or $[22\bar{4}\bar{3}]$ dislocations and PDs, and the associated slip planes along with their *d*-spacing and the angle they make with the (0001) growth plane. Where applicable, top is W representation with ZB equivalent below. 26

1. Objectives

The suitability of a substrate is typically a subjective condition that takes into consideration the lattice constants, elastic properties, thermal expansion coefficients, respective chemistries/reactivities, and relative ease of fabrication of the two juxtaposed materials. A cursory analysis suggests that aluminum nitride (AlN) would be a good candidate as a substrate for aluminum gallium nitride ((Al)GaN), and recently, companies such as HexaTech have been able to grow high quality AlN crystals. While the AlN lattice does not perfectly match gallium nitride (GaN), it is much closer than that of silicon carbide (SiC) or sapphire, and it is chemically very similar to GaN. In addition, the lattice strain caused by the lattice mismatch can be distributed over three dimensions instead of two by using a graded interlayer of $Al_xGa_{1-x}N$, where x varies from $1 \rightarrow 0$ over a finite thickness. Superlattices, which are structures in which the aluminum (Al) composition abruptly changes back and forth between two concentrations, that block the propagation of dislocations can also be grown.

The main objective of this report is to establish a multiscale approach for the simulation of dislocations in (Al)GaN semiconductors. The organization of the report is as follows. After an introduction section, we provide a brief review of dislocations in wurtzite (W) and zincblende (ZB) structures. Next, we present classical molecular dynamics (MD) simulations of dislocations in different slip systems to estimate dislocation velocities as a function of applied stress. The main goal of the classical MD work is to calculate mobility functions for the next microstructural scale of simulations presented in section 5. In that section, different junction configurations are studied using a discrete dislocation dynamics (DDD) simulator, ParaDiS, with different elasticities and a variety of Burgers vector pairs to examine their effects on the junction strengths. Given the complexity of multiple available interacting slip systems, this work focuses on detecting any similarity and differences in junction strengths and results are presented for hexagonal metals. In section 6 of the report, we performed quantum mechanical simulations of atomic and electronic structure of threading edge and screw dislocations in AlGaN in order to understand the structure of the dislocation core and electrical activity of dislocations. Finally, in the last section of the report we present predictions of the possible slip planes in wurtzite (Al)GaN semiconductors based on general crystallographic principles.

2. Introduction

With its large, direct energy gap, E_G, GaN is an important semiconductor. It can be used to fabricate diodes that enable electric vehicles to run more efficiently than they can if they used diodes made from silicon because GaN has a much larger breakdown field. The large value of E_G

also enables GaN diodes to efficiently emit blue/ultraviolet (UV) light that is used to read/write on high density information storage disks. The wavelength of light that is emitted can be tuned by forming solid solutions with other group III elements such as indium for indium gallium nitride (InGaN), or with Al for AlGaN. AlGaN is of particular interest to the Army because it can be made to emit at wavelengths that will sterilize water for troops in the field or at wavelengths that are solar blind—wavelengths from the sun that are screened out by the ionosphere. With its larger $E_{G,}$ a two-dimensional electron gas (2DEG) is formed at the AlGaN/GaN interface when AlGaN films are grown on GaN substrates. These electrons have a mobility, μ, that is larger than it is in the bulk, enabling high electron mobility transistors (HEMTs) that exploit this effect to operate at the GHz frequencies used in radar systems. They can also generate more power for longer distance communication systems than HEMTs made from gallium arsenide (GaAs) both because GaN has a larger breakdown field and a more dense 2DEG. The 2DEG is denser because the AlGaN is in tension due to AlN having a smaller lattice parameter than GaN, since the Al atom is smaller than the gallium (Ga) atom. The tensile strain will generate a positive charge at the AlGaN/GaN interface that attracts electrons. It will also have a denser 2DEG because there is a spontaneous positive charge at the interface due to the nitrides have the hexagonal W structure. In this hexagonal structure, the vertical bond in the sp^3 hybrid bonding structure has a length different than the other three bonds. This causes the center of positive charge to be different than the center of negative charge, which creates a permanent dipole. Because the vertical bond in the III-N is smaller, it too will create a positive charge at the interface. This greatly enhanced carrier concentration in the 2DEG of the HEMTs can be exploited for high power electronic applications, as well as for high power radio frequency (RF) applications, by reducing the on-loss with its greater conductivity. In addition to enabling electric vehicles to operate more efficiently, these HEMTs could be used in high power integrated circuits (HPICs) that could enable micro-grids to operate more efficiently.

However, having different lattice parameters and not having the more traditional cubic ZB crystal structure comes at a price. Having different lattice parameters causes mismatch dislocations to form at or near the interface to compensate for the lattice mismatch when the thickness of the film exceeds its critical thickness, and these dislocations have different structures that slip (move) on different planes. In the case of silicon germanium (SiGe), films are grown in such a way as to minimize the dislocation concentration near the top surface where the SiGe lateral devices used in integrated circuits (ICs) are fabricated (*1*). We would like to learn how to emulate that process for W-AlGaN films because the mismatch dislocations degrade the properties of devices made from these films. To do this, we must determine through theory what the likely initial mismatch dislocation structure looks like and then compute how these dislocations will move through the lattice.

3. Description of the Dislocations

The fundamental bonding element for semiconductors is the sp^3 hybrid shown in figure 1a with the nitrogen (N) anion at the center of a tetrahedron with Ga cations at the four corners. In the cubic ZB structure all of the bond lengths and bond angles are the same (109.5°) and the tetrahedron is a perfect tetrahedron. In the hexagonal W structure, the vertical bond can have any length, but for the nitrides it is shorter than the other three. The base of the inverted tetrahedron shown in figure 1b is an equilateral triangle, and if the atoms represented as hard spheres were allowed to touch, each atom would be surrounded by six others all touching it, as is shown in figure 1c. This is called the close packed plane (*cpp*).

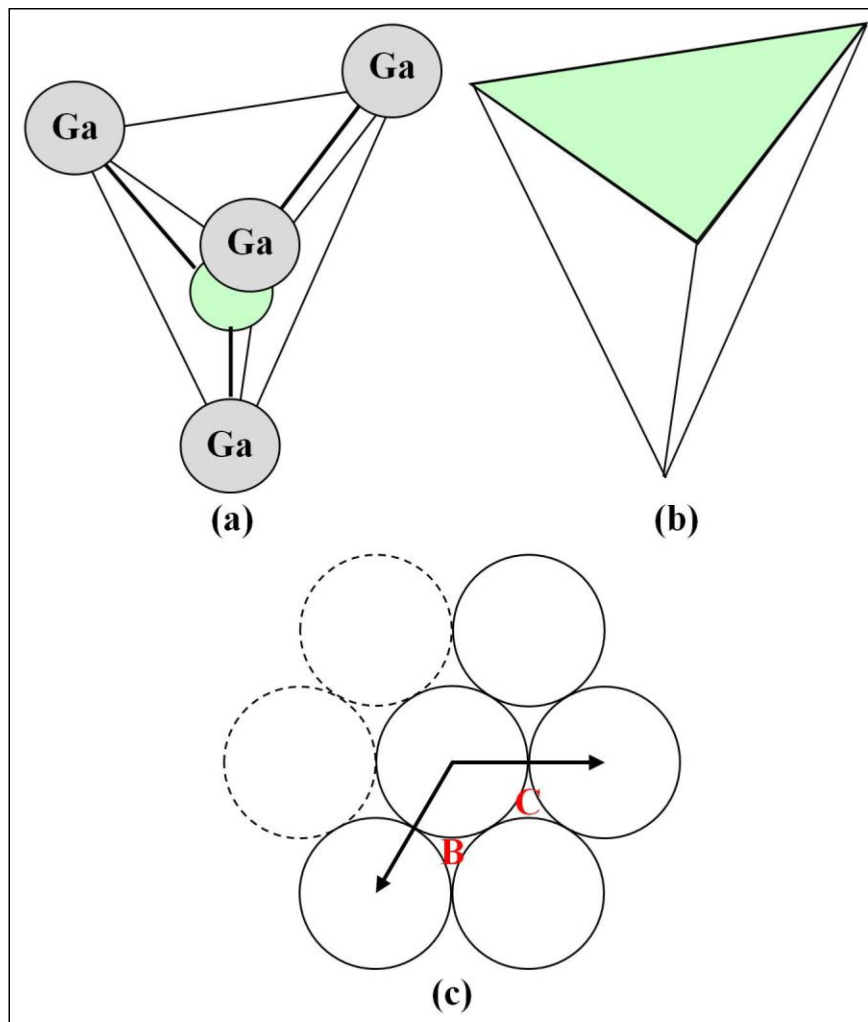

Figure 1. The sp^3 bonding structure typical in most semiconductors. (a) The tetrahedron formed by the four cations that surround the anion inside of it. (b) Same, with ions not visualized. (c) A *cpp* and the B and C sites for the *cpp* that can lie above it.

There is only one such plane in the W structure, and it is parallel to the base of the inverted pyramid in figure 2a. Given that it is parallel to the base of the W unit cell, as shown figure 2b, it is also parallel to the (0001) plane using the Miller indices notation for hexagonal crystals and the 3-indices notation for the other crystal systems, making it the $(001)_H$ plane. The tip of the inverted tetrahedron lies at the origin of the unit cell and the three other atoms that form the base of the unit cell are the red spheres in figure 2b.

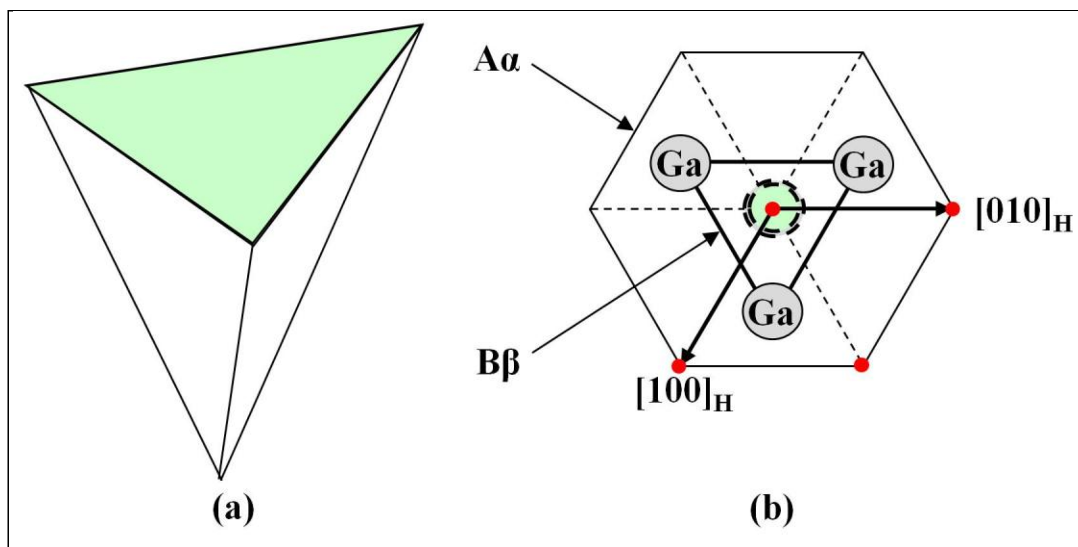

Figure 2. (a) The *sp*^{3} tetrahedron in the hexagonal W structure with its green base parallel to the (0002) *cpp*. (b) The stacking structure of W crystal.

The base of the tetrahedron, which is a *cpp* parallel to the base, has the same planar structure as the one in the base, but it is shifted in the plane of the paper so the atoms lie directly above the points marked with a B in figure 1c. The next plane up that contains Ga atoms lies directly above those in the plane of the paper, and it lies in the plane that forms the top of the unit cell. One could therefore say that the stacking sequence for the *cpps* for the W structure is ABAB…—the Ga atoms at the eight corners of the unit cell and the yellow atom in the base of the tetrahedron that lies inside of the unit cell are said to form a hexagonal close packed (*hcp*) unit cell. The cell is defined by the basis vectors, $\mathbf{a_1}$ and $\mathbf{a_2}$ that are of equal length, a_H, lie in the *cpp*, and make an angle of 120° with each other. The third basis vector, $\mathbf{a_3}$, is normal to the *cpp* with a length, c. The ratio, $\gamma = c/a_H$ is often used to characterize the cell. If all of the bond lengths of the *sp*^{3} hybrid bonds are of equal length, $\gamma = \sqrt{8/3} = 1.633$. Since the N atom lies directly above a Ga atom they have an identical packing sequence, but to distinguish N atoms from Ga atoms, Greek letters are used to describe their stacking sequence. The overall stacking sequence for all of the *ccps* containing atoms in the W structure is therefore AαBβAαBβ…, as seen in figure 2b. Because the plane containing the Ga atoms in the base of the tetrahedron cuts the vertical axis of the unit cell, the c-axis, in half, it is the (0002) $[(002)_H]$ plane.

As one can see in figure 3a, the regular tetrahedron depicting where the atoms lie in the cubic ZB structure can be created by putting Ga atoms at every other corner of a cube and a N atom at the center of this cube. The unit cell for the ZB structure can be formed by stacking eight of these cubes to form a cube with an edge twice as long as the original cube and every other small cube contains an N atom at its center, as is shown in figure 3b.

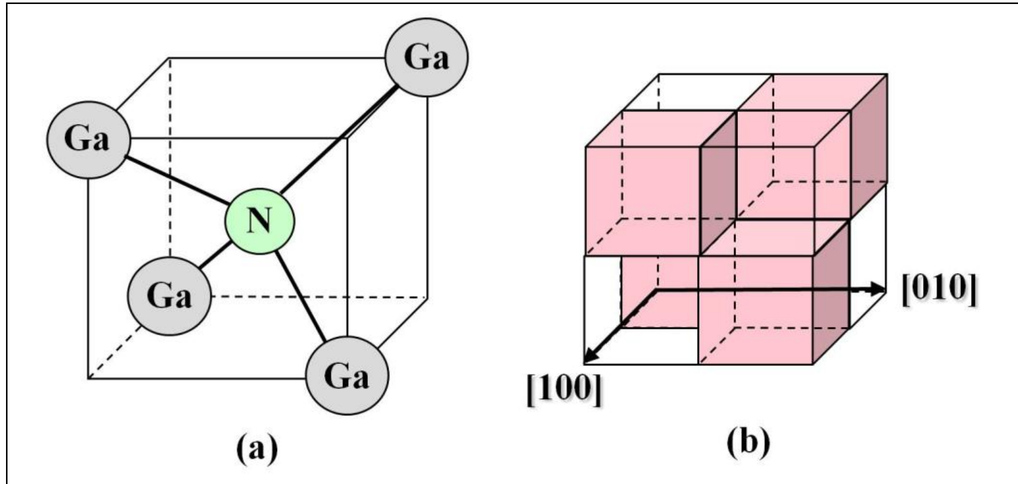

Figure 3. (a) The cube used to construct the sp^3 tetrahedron in a ZB cubic unit cell and (b) the cubic ZB unit cell.

The Ga atoms lie at the eight corners of the cube and at each of the six faces; this unit cell is called a face centered cubic (*fcc*) unit cell. The basis vectors $\mathbf{a_1}$, $\mathbf{a_2}$, and $\mathbf{a_3}$ that are used to define the unit cell are the edges of the cube of length, *a*. The tip of the tetrahedron again lies at the origin, and its base is perpendicular to the $[111]$ direction so it is parallel to a (111) plane. It in fact lies in the (111) plane, which is identical to the (0002) W plane. Between the Ga atoms at the origin and the one lying directly above it along the $[111]$ body diagonal of the unit cell at the opposite corner, there are two other tetrahedra whose bases are *cpps* that are parallel and identical to the (111) planes. Looking down the $[111]$ direction the Ga atom at the tip of the tetrahedron formed in the smaller cube in the upper left-hand corner lies above the point B in figure 1c. The tip in the tetrahedron formed in the smaller cube opposite a face diagonal from the cube at the origin lies above the point C marked in figure 1c. One can make the same argument for the N atoms because they lie directly above Ga atoms so the stacking of the *cpps* in the ZB structure is said to be AαBβCγAα….

As a general rule the *cpp* is the plane along which edge dislocations most easily move because atoms in these planes are the furthest apart from atoms in an identical plane above it, making it easier for them to glide over each other. Thus, they are called the primary slip plane, **h**. As shown in figure 4a, there are four non-parallel $\{111\}$ planes—the (111), $(1\bar{1}1)$, $(\bar{1}\bar{1}1)$, and $(\bar{1}11)$—that are identical. The slip direction and length (the Burgers vector, **b**) is usually the shortest lattice vector in the slip plane, which for the *fcc* unit cell is a $\langle \frac{1}{2}\ 0\ -\frac{1}{2} \rangle$ type direction that lies in the slip plane, as shown in figure 4b. The line that separates the slipped portion of the

crystal and lies in the slip plane (the dislocation line, $\boldsymbol{l}$) can be a $\langle 01\bar{1}\rangle$ direction. If $\boldsymbol{l}$ is this type direction (and it usually is in ZB structures), then the dislocation is said to be a 60° dislocation because the angle between **b** and $\boldsymbol{l}$ is 60°. If $\boldsymbol{l}$ is parallel to a $\langle\bar{1}2\bar{1}\rangle$ type direction, then it is an edge dislocation because **b** is normal to $\boldsymbol{l}$. It is the edge component of **b** that compensates for the lattice mismatch. The component of **b** ∥ $\boldsymbol{l}$ is the screw component.

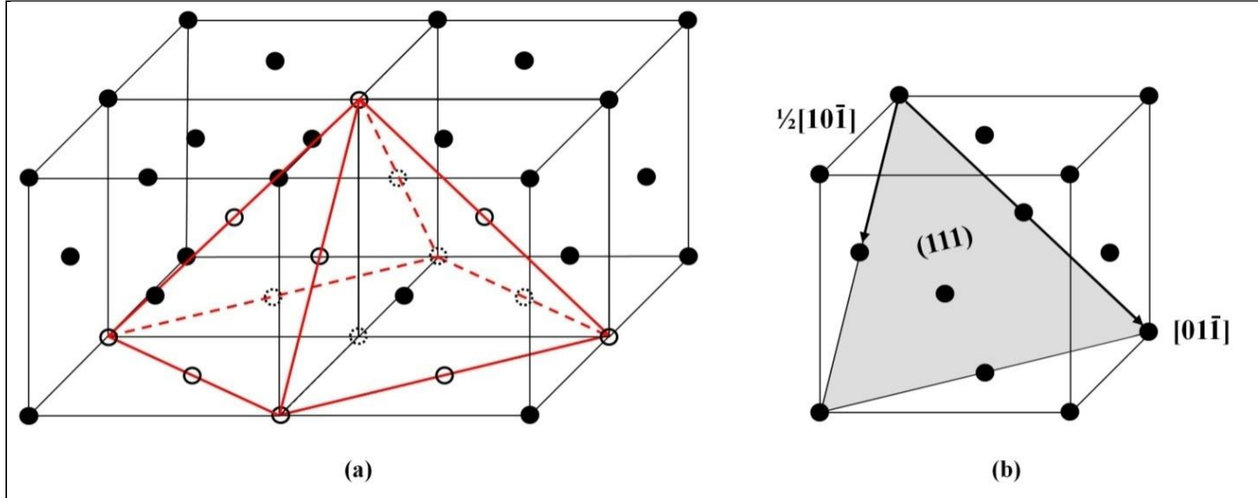

Figure 4. (a) The four equivalent $\{111\}$ type slip planes in the cubic ZB structure. (b) The $\left[\frac{1}{2}\;0\;-\frac{1}{2}\right]$ Burgers vector and the $[01\bar{1}]$ dislocation line for the 60° dislocation line in the (111) plane of a cubic ZB structure.

4. Classical Molecular Dynamics Simulations of Dislocations in GaN

We have performed classical MD simulations to obtain dislocation velocities as a function of applied stress in order to calculate mobility functions for various slip systems. In these simulations, shear is applied to a crystal system containing a single edge dislocation (i.e., reference 2). In this work, we focus on three slip systems containing pure edge dislocations.

All simulations were performed using the Large-Scale Atomic/Molecular Massively Parallel Simulator (LAMMPS) computer code (*3*). The interatomic potential is a bond order potential developed for GaN (*4*) using the Tersoff-Brenner formulation (*5*), which was fit using both experimental data and results from density functional theory (DFT). It accurately reproduces a number of structural and material properties of Ga, N, and GaN, and the absence of long-range forces allows for relatively fast simulations. All the simulations presented here are performed in the NVT ensemble at a temperature of 1300 K, with a timestep of 1 fs.

We begin by generating a single crystal oriented such that the Burgers vector, **b**, of the subsequent dislocation will point in the *x*-direction, while the dislocation line, $\boldsymbol{l}$, will align with the *y*-axis. The initial single crystals of wurtzite GaN contain around 1.4 million atoms, with dimensions of approximately 250 × 250 × 250 Å. A single dislocation is introduced by the

trench method (*6*), represented in figure 5. As seen in figure 5a, where all atomic positions are projected onto the plane, two half planes of atoms along the *z*-direction are removed from the lower half of the crystal. Due to the mismatch in the number of half-planes, periodic boundaries are only implemented in the *x*- and *y*-directions, while the *z*-surfaces are free. Furthermore, atoms within 10 Å of the top and bottom free surfaces are constrained to move in the *xy*-plane as these are the atoms through which shear will be applied to the system after relaxation. The system is equilibrated for 20 ps, resulting in the configuration seen in figure 5b. The trench has closed, leaving a dislocation near the middle of the simulation cell, shown in expanded view in figure 5c.

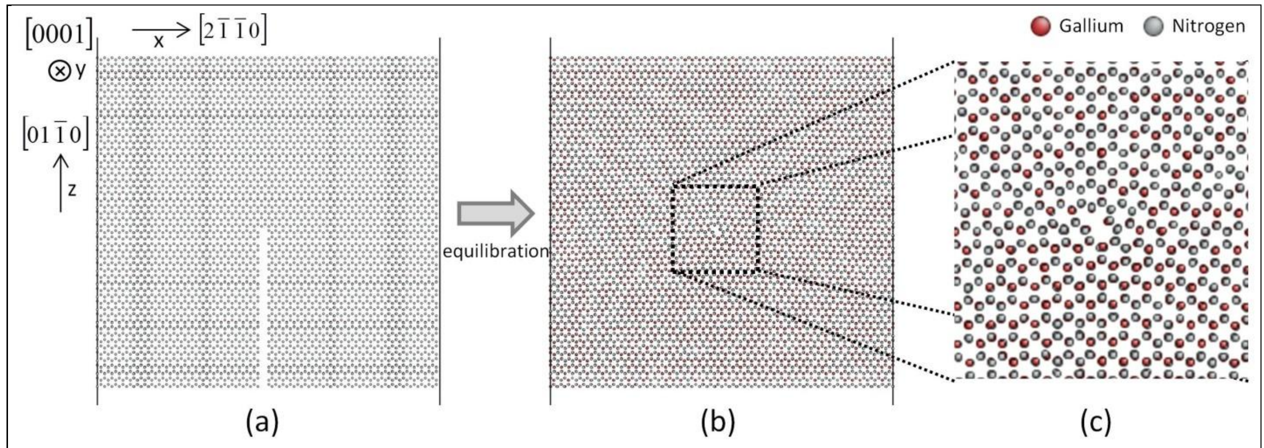

Figure 5. Method of generating a dislocation in a single crystal: (a) two half planes are removed from the lower half and after equilibration, (b) a dislocation remains near the center of the system, a close-up of which is seen in (c).

Once equilibrated, the system is deformed by applying shear in a stress controlled manner (*7*), as depicted in figure 6. This is achieved by applying an additional force to those atoms that were constrained to move in the *xy*-plane during equilibration (the "top" and "bottom" regions in figure 6). Atoms in the top region are given a force in the positive *x*-direction and those in the bottom in the negative *x*-direction. The force on each Ga atom is scaled by a factor of 4.9778 compared to the force on N atoms to account for their larger mass ($m_{Ga}/m_N = 4.9778$), and to maintain the wurtzite crystal structure in the top and bottom regions. Furthermore, considering that atoms were removed from the bottom region in order to generate the dislocation, the force on Ga (N) atoms in the bottom region is larger than the force on Ga (N) atoms in the top region. The forces are scaled such that the total force on all the atoms in each region is equivalent. The applied stress is simply calculated as the total force on the top (or bottom) region divided by the *xy*-area of the simulation region.

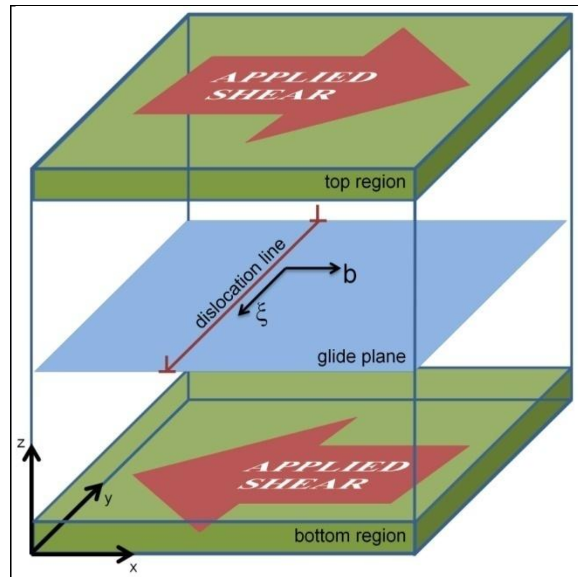

Figure 6. A depiction of the simulation technique to measure dislocation velocity as a function of applied stress.

If the applied stress is high enough, the dislocation will begin to glide, as shown in figure 7. In this figure, only atoms with other than four nearest neighbors are visualized. The initial position of the dislocation line is shown near the center of the simulation region in figure 7a, and its subsequent position after 2 ns (figure 7b) is to the right of its initial position. The pairs of atoms that appear at some distance from the dislocation are due to thermal fluctuations and do not represent defects in the single crystal.

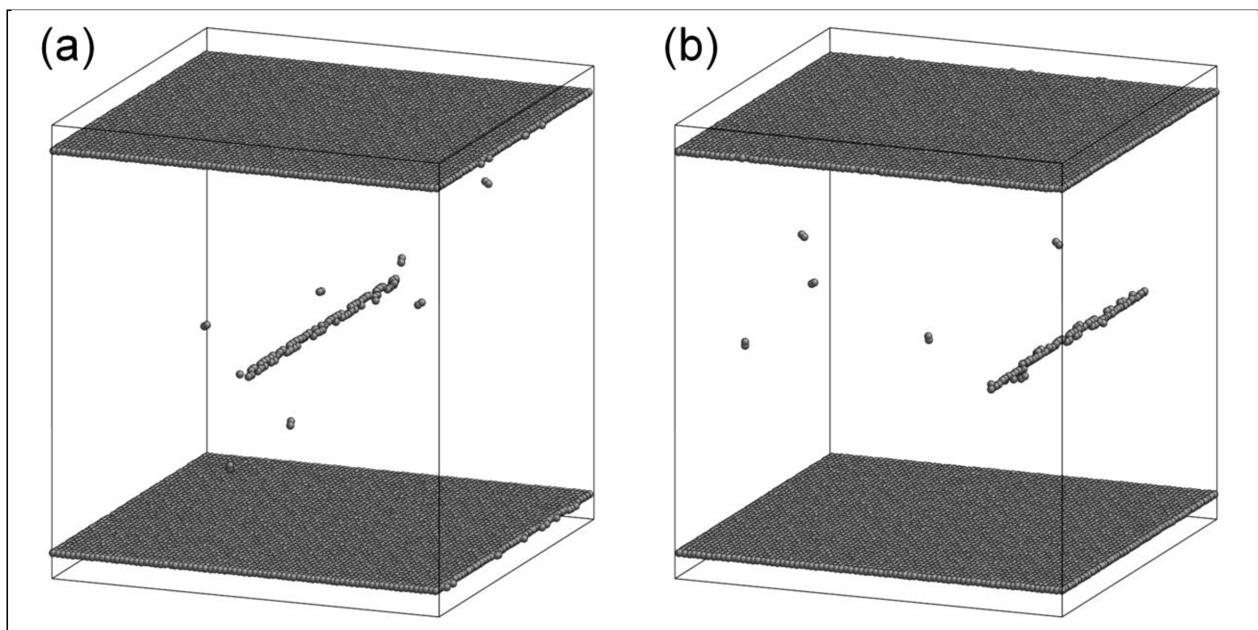

Figure 7. Example of dislocation glide. The visualization software is AtomEye (*8*).

Once the dislocation begins to glide, there is typically a rapid acceleration before the dislocation settles into an equilibrium velocity. Once this state is reached the simulation can run indefinitely since periodic boundaries parallel to the glide plane allow the dislocation to pass entirely through the system and re-enter on the other side. The x-position of the dislocation can be determined by identifying and averaging those atoms with a coordination number other than four. The position of the dislocation as a function of time over a 1000 ps (1 ns) interval is fitted to a line in order to calculate the velocity, as shown in figure 8. We also ensure that the dislocation remains coherent throughout the length of the simulation since at very high stress the dislocation core can become unstable and either spread or dissociate. The velocity of the dislocation is simply equal to the slope of the fitted line.

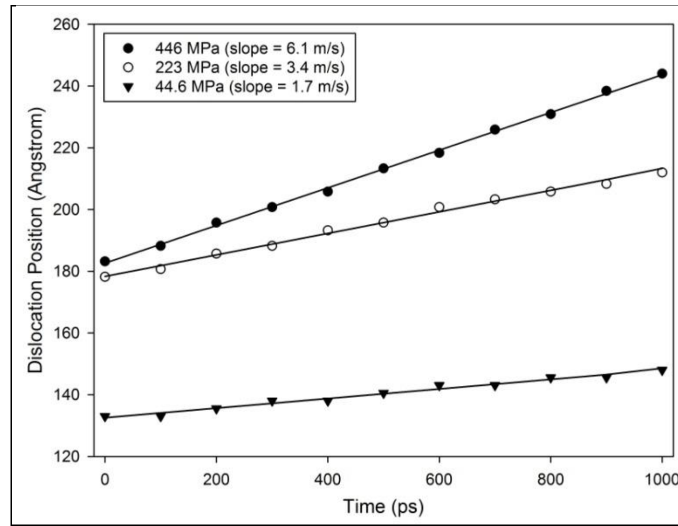

Figure 8. Position of dislocation as a function of nominal time for three different values of applied stress.

The three slip systems studied in this work are all pure edge, with a Burgers vector equal to the lattice parameter a = 3.160 Å for this potential at T = 1300 K. Figure 9 shows the velocity as a function of applied stress on a logarithmic plot for the three slip systems identified. We observe relatively low values of dislocation velocities corresponding to very high values of applied stress, at least compared to previous MD studies of metallic systems where velocities on the order of 100 m/s are observed for stresses on the order of 100 MPa (*2*). The behavior of the $(0001)[\bar{1}\bar{1}20]$ and $(1\bar{1}00)[\bar{1}\bar{1}20]$ slip systems is similar, with the former having slightly more mobile dislocations. The dislocations in the $(1\bar{1}01)[\bar{1}\bar{1}20]$ slip system are much less mobile, but above a critical stress of approximately 3 GPa the dislocation velocity increases rapidly.

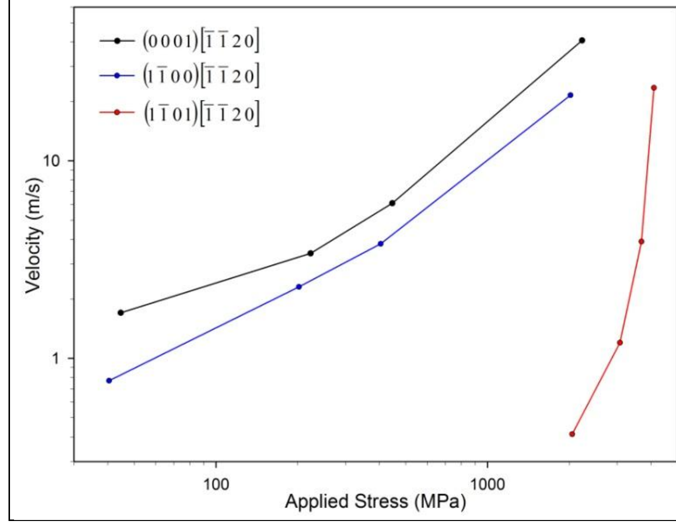

Figure 9. Log-log plot of dislocation velocity as a function of applied stress for the three slip systems identified in the legend.

5. Non-coplanar Binary Dislocation Junctions in Hexagonal Close-packed Crystals

Study of dislocation junction strengths in *hcp* crystals is important to understand and control the density of deleterious dislocations in wide band-gap wurtzite semiconductors. This is due to the fact that junction formation is a key entanglement mechanism leading to high dislocation density, and *hcp* structures are the foundation of wurtzite semiconductors. Different junction configurations are studied using a DDD simulator, ParaDiS (*9*), with different elasticity and a variety of Burgers vector pairs to examine their effects on the junction strengths. Given the complexity of multiple available interacting slip systems, this work focuses on detecting any similarity and differences in junction strengths.

5.1 Approach

For each set of interacting dislocation slip systems, first an equilibrium binary junction is formed along the intersecting edge of two different slip planes from two intersecting straight dislocations with no net stress field. The dislocation is inserted onto the center of each plane—a straight dislocation making a 30° angle to the intersection edge (*10*). The Burgers vector pairs are selected such that it is energetically favorable to form a junction. All the vectors and planes are described in the code using the 3-index notation (*11*). Table 1 is a list of different sets of interacting slip systems investigated in this work, along with the corresponding 4-index Miller notations. The interactions are also schematically illustrated in figure 10. Table 1 also includes the Burgers vectors, categorized as $\langle a \rangle$ type, $\frac{1}{3}\langle 11\bar{2}0 \rangle$, $\langle c \rangle$ type, $\langle 0001 \rangle$, or $\langle a + c \rangle$ type, $\frac{1}{3}\langle 11\bar{2}\bar{3} \rangle$. The Burgers vector and line direction of each resultant junction are listed in table 2.

Table 1. Slip planes and Burgers vectors.

	Slip plane		Burgers vector		
	4-index	3-index	4-index	3-index	type
(a)	$(0\ \ 0\ \ 0\ \ 1)$	$\left(0\ \ 0\ \ \frac{c}{a}\right)$	$\frac{1}{3}[1\ \ \bar{2}\ \ 1\ \ 0]$	$\left(\frac{1}{2}\ \ \frac{\sqrt{3}}{2}\ \ 0\right)$	$< a >$
	$(0\ \ 1\ \ \bar{1}\ \ 0)$	$(\sqrt{3}\ \ 1\ \ 0)$	$\frac{1}{3}[\bar{2}\ \ 1\ \ 1\ \ 0]$	$\left(\frac{1}{2}\ \ -\frac{\sqrt{3}}{2}\ \ 0\right)$	$< a >$
(b)	$(\bar{2}\ \ 1\ \ 1\ \ 2)$	$(-\sqrt{3}c\ \ 3c\ \ -2\sqrt{3}a)$	$\frac{1}{3}[2\ \ \bar{1}\ \ \bar{1}\ \ 3]$	$\left(-\frac{1}{2}\ \ \frac{\sqrt{3}}{2}\ \ \frac{c}{a}\right)$	$< a{+}c >$
	$(0\ \ 1\ \ \bar{1}\ \ 0)$	$(\sqrt{3}\ \ 1\ \ 0)$	$\frac{1}{3}[\bar{2}\ \ 1\ \ 1\ \ 0]$	$\left(\frac{1}{2}\ \ -\frac{\sqrt{3}}{2}\ \ 0\right)$	$< a >$
(c)	$(\bar{2}\ \ 1\ \ 1\ \ 2)$	$(-\sqrt{3}c\ \ 3c\ \ -2\sqrt{3}a)$	$\frac{1}{3}[2\ \ \bar{1}\ \ \bar{1}\ \ 3]$	$\left(-\frac{1}{2}\ \ \frac{\sqrt{3}}{2}\ \ \frac{c}{a}\right)$	$< a + c >$
	$(0\ \ 1\ \ \bar{1}\ \ 0)$	$(\sqrt{3}\ \ 1\ \ 0)$	$[0\ \ 0\ \ 0\ \ \bar{1}]$	$\left(0\ \ 0\ \ -\frac{c}{a}\right)$	$< c >$

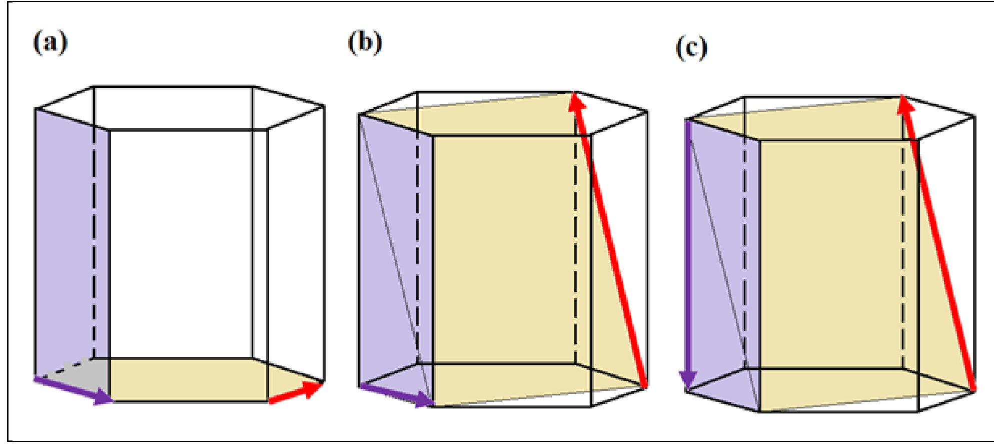

Figure 10. Illustration showing the selected different interacting slip systems: The purple arrows represent the Burgers vectors for the dislocation on the $(01\bar{1}0)$ plane (also in purple). The red arrows represent the Burgers vectors for the dislocation on the (0001) plane in case (a) and on the $(\bar{2}112)$ plane in cases (b) and (c), respectively.

Table 2. The Burgers vectors and directions of the resultant binary junctions.

	Burgers vector		Junction direction	
	4-index	3-index	4-index	3-index
(a)	$\frac{1}{3}[\bar{1}\ \bar{1}\ 2\ 0]$	$[1\ 0\ 0]$	$\frac{1}{3}[\bar{2}\ 1\ 1\ 0]$	$\left(\frac{1}{2}\ -\frac{\sqrt{3}}{2}\ 0\right)$
(b)	$[0\ 0\ 0\ 1]$	$\left(0\ 0\ \frac{c}{a}\right)$	$\frac{1}{3}[2\ \bar{1}\ \bar{1}\ 3]$	$\left(-\frac{1}{2}\ \frac{\sqrt{3}}{2}\ \frac{c}{a}\right)$
(c)	$\frac{1}{3}[2\ \bar{1}\ \bar{1}\ 0]$	$\left(-\frac{1}{2}\ \frac{\sqrt{3}}{2}\ 0\right)$		

The junction strengths are then examined by loading each equilibrium junction with a 3×3 applied stress tensor, $\boldsymbol{\sigma}$, calculated as

$$\boldsymbol{\sigma} = \sigma_1 \mathbf{S_1} + \sigma_2 \mathbf{S_2} + \sigma_3 \mathbf{S_3} \tag{1}$$

where $\boldsymbol{S}_i$ (i = 1~3) are the 3×3 orthogonal projection matrices for the two interacting dislocations (i = 1, 2) and the junction (i = 3), and σ_1, σ_2, and σ_3 are their respective scalar resolved shear stresses in units of MPa. Here, $\boldsymbol{S}_i$ are calculated from the Schmid tensors (*12*)

$$\mathbf{s}_i = \left(\frac{\mathbf{b}_i}{|\mathbf{b}_i|} \otimes \frac{\mathbf{n}_i}{|\mathbf{n}_i|} + \frac{\mathbf{n}_i}{|\mathbf{n}_i|} \otimes \frac{\mathbf{b}_i}{|\mathbf{b}_i|} \right) \tag{2}$$

$$S_i : s_i = 1 \tag{3}$$

$$S_i : s_j = 0, i \neq j \tag{4}$$

such that a stress applied on one plane would not contribute any resolved stress on the other. In equation 2, $\boldsymbol{b}_i$ are the Burgers vectors and $\boldsymbol{n}_i$ are the unit normal vectors.

In the simulation, the coefficient σ_3 in equation 1 is set to zero so that $\boldsymbol{\sigma} = \sigma_1 \boldsymbol{S}_1 + \sigma_2 \boldsymbol{S}_2$. This is to prevent the junction from bowing out and ensure a straight unzipping along the straight junction line. For each specified σ_1/σ_2 ratio, the junction is loaded repeatedly by the stress tensor, $\boldsymbol{\sigma}$, with an incrementally increasing magnitude. For each stress increment, the junction is allowed to equilibrate for a total of 30,000 timesteps until the junction is completely dissolved and the initially locked dislocations become two separate glissile dislocations again. The critical stress pairs (σ_{1c}, σ_{2c}) obtained from all specified σ_1/σ_2 ratios are then normalized by a scaling factor

$$\sigma_{i,c} = \sigma'_{i,c} \left[\frac{\mu}{L(1-\nu)} \ln\left(\frac{R}{r_o} \right) \right] \tag{5}$$

and the pairs of (σ'_{1c}, σ'_{2c}) constitute a junction yield surface. In equation 5, the slip plane index is i (= 1, 2), L is the initial length of intersecting dislocations, μ is the shear modulus, v is the Poisson's ratio, and R and r_o are the outer and inner cut-off radii for linear elasticity, respectively. In this work, the σ_2 refers to the resolved stress on the $(01\bar{1}0)$ plane in all cases. The σ_1 corresponds to the stress applied on the (0001) plane for case (a) and the $(\bar{2}112)$ plane for cases (b) and (c). The core radius, r_o, is approximated as equivalent to the lattice spacing of the basal plane.

5.2 Formation of Equilibrium Junctions

The resultant properties of equilibrium junctions are summarized in table 3. They include the equilibrium length, L_e (in the unit of a where a is the lattice spacing on the basal plane), the approximate total energy reduction, ΔE, and the arm orientations, ψ_1' and ψ_2', measured from the intersection edge to the arms. For all cases studied here, the ψ_2' refers to the orientation on the $(01\bar{1}0)$ plane. However, the ψ_1' refers to the (0001) plane in case (a) but to the $(\bar{2}112)$ plane in cases (b) and (c). When the junction starts to form, it continues growing until all forces at the triple nodes are balanced. As shown in case (c), the results indicate that it is most energetically favorable to form the $(\bar{2}112)/(01\bar{1}0)$ junction with the interacting Burgers vectors of $\langle a + c\rangle$ and $\langle c\rangle$. In case (a), interactions from the Burgers vector pairs of the same type would result in identical junction arm orientations (i.e., $\psi_1' = \psi_2'$). On the contrary, in cases (b) and (c) the Burgers vector pairs of different types would lead to different arm orientations on different planes (i.e., $\psi_1' \neq \psi_2'$). In fact, the junctions studied in this work are associated with the prismatic $(01\bar{1}0)$ plane intersecting with different planes—the (0001) plane for case (a) and the $(\bar{2}112)$ plane for cases (b) and (c). Therefore, the equilibrium length and arm orientations in cases (b) and (c) are only sensitive to the choice of Burgers vector on the $(01\bar{1}0)$ plane. Our findings of different junction lengths corresponding to different slip systems are also consistent with an earlier report by Yoo et al. (*13*).

Table 3. Properties of the equilibrium junctions.

Case	Material	L_e	ΔE (%)	ψ_1'/ψ_2'
(a)	Be	23,323	50	60°/60°
	Mg	23,769	50	62°/62°
(b)	Be	21,698	45	54°/65°
	Mg	16,145	43	45°/64°
(c)	Be	31,311	83	88°/75°
	Mg	26,029	84	78°/60°

5.3 Junction Unzipping and Yield Surfaces

In principle, the junction unzipping is carried out via Frank-Read bow out by the resolved stresses (*14–16*). Therefore, the critical breaking stress has a linear relation with the elastic constants. As anticipated, the critical stress pairs, (σ_{1c}, σ_{2c}), for beryllium (Be) are one order of magnitude greater than those for magnesium (Mg) with all specified σ_1/σ_2 ratios. Figures 11–13

are the yield surface plots for all cases studied. The data points are comprised of the normalized stress pairs, (σ'_{1c}, σ'_{2c}).

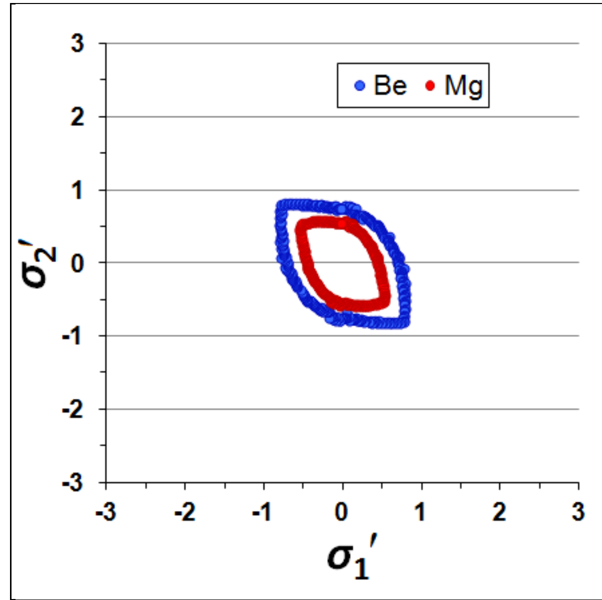

Figure 11. The yield surfaces for case (a). σ_1' and σ_2' are the normalized resolved applied stresses on the (0001) and the $(01\bar{1}0)$ planes, respectively. The junction is oriented along $[1\ \sqrt{3}\ 0]$, equivalent to $[\bar{2}110]$ in the 4-index notation.

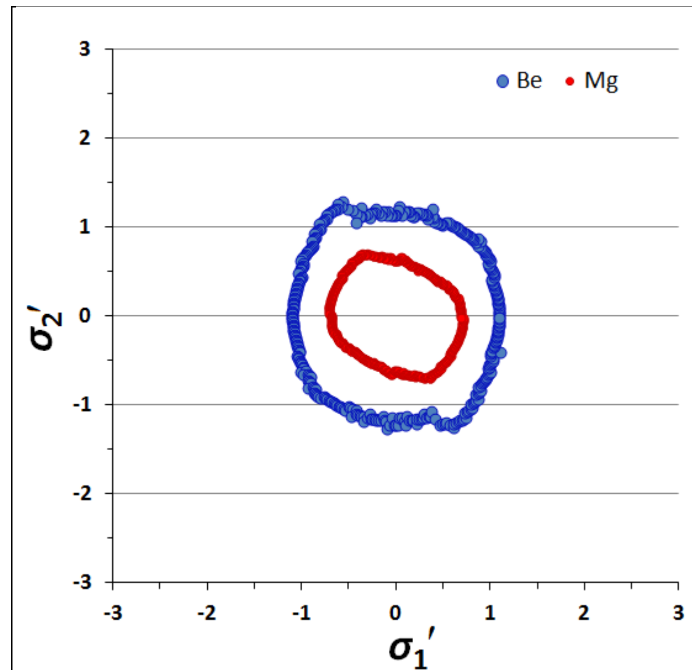

Figure 12. The yield surfaces for case (b). σ_1' and σ_2' are the normalized resolved applied stresses on the $(\bar{2}112)$ and the $(01\bar{1}0)$ planes, respectively. The junction is oriented along $[1 - \sqrt{3}\ 0]$, equivalent to $[\bar{2}110]$ in the 4-index. notation.

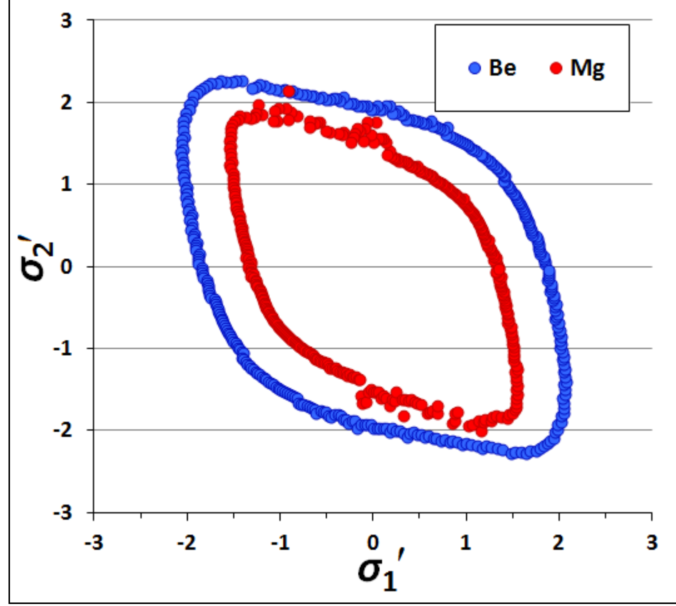

Figure 13. The yield surfaces for case (c). σ_1' and σ_2' are the normalized resolved applied stresses on the $(\bar{2}112)$ nd the $(01\bar{1}0)$ planes, respectively. The junction is oriented along $[1 - \sqrt{3}\ 0]$, equivalent to $[\bar{2}110]$ in the 4-index notation.

The yield surfaces in all cases are symmetric, which is similar to those in *fcc* crystals (*17–18*). The symmetry can be attributed to the symmetric configuration of the initial equilibrium junction and the linear mobility used in the code. To validate the anticipated symmetry, we have run simulations for all the data points needed to compose the closed envelope. The yield surfaces are also elongated along a straight line, $\sigma_2 = m\sigma_1$, that represents the major axis where m is the slope of that line. The positive or negative sign of m depends on the choice of slip planes used to create the junction and the consequence that choice has on the orthogonal Schmidt tensor $\boldsymbol{S}$. The uniformity upon scaling with equation 5 reaffirms the sensitivity to the elastic constants of the material as mentioned previously.

As depicted in figures 11–13, the inclination of yield surfaces does not vary significantly among different junction configurations and slip systems. For the $(0001)/(01\bar{1}0)$ junction in case (a), the size of yield surfaces are significantly smaller and the shapes resemble those in *fcc* crystals (*17*). This can be attributed to all the Burgers vectors involved in this case are of the $\langle a \rangle$ type on the basal plane. This type of Burgers vector corresponds to the shortest translation vector on the sole close-packed slip plane for *hcp* crystals and resembles the $\langle 110 \rangle$ glide on the $\langle 111 \rangle$ slip planes for *fcc* crystals (–). Moreover, the junction in case (a) is also 60° oriented to its Burgers vector, which has the same orientation as those for *fcc* crystals.

The role of Burgers vectors is more complex in cases (b) and (c). Unlike case (a), the shape and size of yield surfaces would differ from those of *fcc* crystals when the interacting Burgers vector

pairs are of different types and magnitudes. The junction property can also change based on the interacting Burgers vector. When a $\langle c \rangle$ type Burgers vector is involved in the interaction, the resultant junction tends to have a larger yield surface than when an $\langle a \rangle$ type Burgers vector is used. The junction in case (c) is also a pure edge dislocation. By comparing case (b) with cases (a) and (c), the yield surface is more elongated for junctions having more edge part than those having more screw part. This finding is similar to Capolungo's report for junctions in Mg (–) despite a small difference in his normalization factor from that used here.

The size of the yield surfaces evidently depends on the elastic constants, especially the ratio of $\mu/(1-\nu)$. Although the difference in the order of magnitude for the critical unzipping stresses between Be and Mg can be largely eliminated via normalization, the differences are still dominated by the term containing Poisson's ratio, $(1-\nu)$. This results in larger yield surfaces for Be than for Mg in all cases. Overall, the yield surfaces in case (c) are much larger than those in cases (a) and (b) for both Be and Mg. This can be attributed to the large total energy reduction by junction formation (80%) for case (c), in comparison to at most 50% reduction for other cases. This relation is similar to Dupuy and Fivel's finding (*17*) that a greater reduction in the total dislocation energy leads to a stronger junction.

5.4 The Effect of Dislocation Length on Critical Unzipping Stresses

We have also performed simulations to verify the accuracy of our results and the independence of yield surface to the initial dislocation lengths, even though previous studies on junctions in *fcc* crystals suggested similar properties (*21, 22*). In principle, the magnitude of the critical resolved stresses is reduced accordingly with increasing dislocation length. Figure 14 displays the yield surface of the $(0001)/(01\bar{1}0)$ junction in Be by varying L twice and ten times the original length of 40,000a, where L is the initial dislocation length, and after scaling by $\ln(L)/L$. As shown in the figure, the shape of the yield surfaces, namely the junction strength, is independent of the dislocation length.

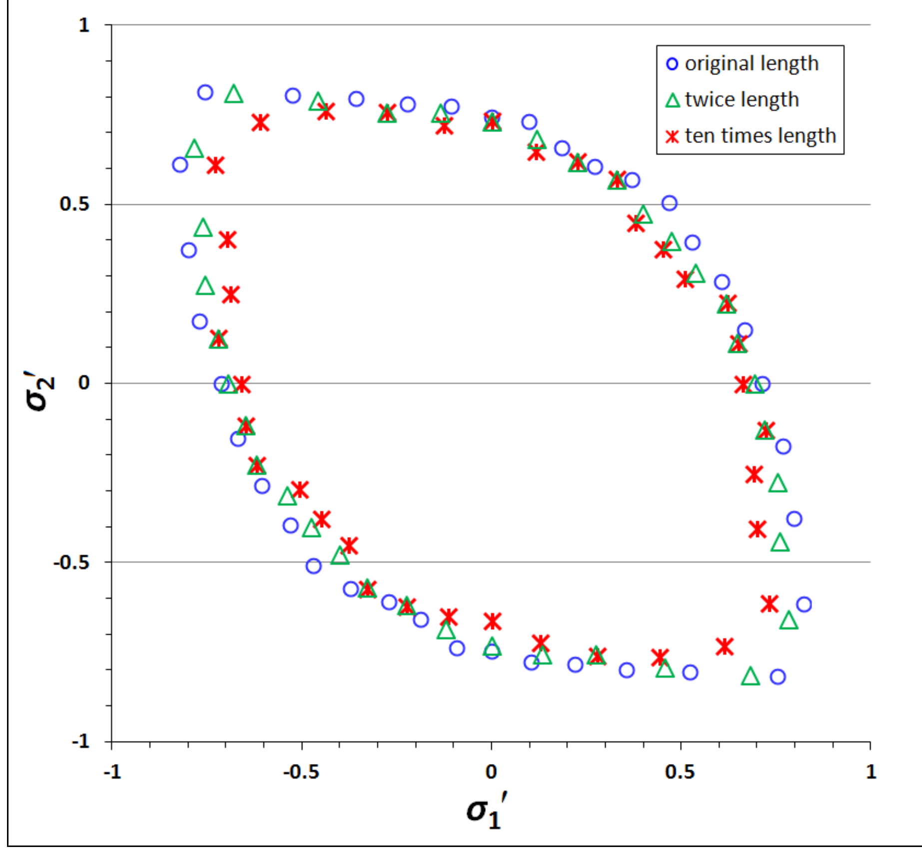

Figure 14. The yield surfaces for the junction in Be in case (a) with varying initial dislocation lengths, *L*. The junction is oriented along $[1\ -\sqrt{3}\ 0]$, equivalent to $[\bar{2}110]$ in the 4-index notation.

5.5 Wurtzite GaN

We have successfully studied different representative junction strengths in *hcp* crystals via DDD simulations using the ParaDiS code. In this section, we summarize future directions and needs for extending and improving upon the present results. Because the current version of the code was originally designed for modeling perfect dislocations in bulk *hcp* crystals, several slip systems that are important to wurtzite but do not exist in *hcp* crystals are not included, such as the *a*-planes $\{\bar{1}2\bar{1}0\}$, the *r*-plane $\{1\bar{1}02\}$, and the $\langle 1\bar{1}00\rangle$ type Burgers vectors (*23*). In addition, partial dislocations can exist in wurtzite crystals (*24, 25*) and have been found frequently in III-V wurtzite semiconductors in experiments (e.g., reference 26). Furthermore, experimental findings have also indicated a possible dependence of dislocation velocity on the slip systems.

Therefore, the linear mobility law and the weighting factors accounting for the variations of slip planes used in the simulations in this work may not sufficiently reflect the actual dislocation dynamics in nitride-derived wurtzite crystals. In addition, an offset in the lattice spacing may need to be taken into account to model wurtzite materials. The manner in which all these can be suitably represented in ParaDiS requires more careful investigation. In summary, continuing

efforts are necessary, like implementation of additional slip systems and their resultant possible cross slips, nonlinear mobility laws, structure-based core radii via MD simulations, and the lattice spacing adjustment reflecting the compound structure, etc.

6. Quantum Mechanical Simulations of Dislocations in AlGaN

The ternary semiconductor AlGaN in the hexagonal phase is not only an important material for substrates and transition layers, but it is also an important part of electronic devices like HEMTs. A nanolayer of AlGaN over GaN provides extra 2DEG charge density because of the piezoelectric effect of the AlGaN layer. The higher concentration of Al leads to a stronger piezoelectric effect and higher charge density, but the system is not stable above 28 at.% of Al. The structure of the ternary system $Al_xGa_{1-x}N$ is still not well understood. There is a high energy penalty for Al atoms to be on a N site, but the distribution of Al atoms around the extended defects is an open question.

The objective of this section is to understand the details of atomic distribution around threading edge and screw dislocations in ternary random semiconductors, and estimate the electrical activity of the states associated with atoms in the dislocation's core. We model the structure of the ternary system with 25 at.% of Al using quantum mechanical methods and the ideas of evolutionary algorithm (*27*).

We performed first principles simulations of edge and screw dislocations in the basal plane of AlGaN. In order to provide periodical boundary conditions, we needed to use a dislocation dipole. The crude model of the dislocations was created using MD with the same potentials as in section 4. The models of the dislocation dipoles in wurtzite GaN consisting of 296–340 atoms were optimized using DFT and projected augmented plane waves as implemented in the package Vienna Ab-Initio Simulation Package (VASP) (*28*). Total energy of the system (converged with an accuracy of 10^{-6} eV, a 500-eV cut-off energy, and two irreducible k-points) was used as a fitting function in genetic algorithm. We developed a shell script to model evolution of several generations of the system with the same job ID on Department of Defense (DoD) high-performance computers. The first generation is produced by a random-number generator. Among the locally optimized structures, a certain number of the worst ones are rejected, and the remaining structures participate in creating the next generation through heredity, permutation, and mutation operations chosen with a specified weight. Selection probabilities for variation operators are derived from the rank of their fitness (i.e., their VASP calculated free energies). The permutation operator is essentially switching the identities of two or more atoms in a structure, while mutation is a random change of the cell vectors and/or atomic positions. During a heredity operation, new structures are produced by matching slices (chosen in random directions and with random positions) of the parent structures.

As seen in figure 15, Al atoms prefer to be far from the dislocation core in both structures. There might be a straightforward physical explanation of this trend. The Al-N bond in wurtzite AlN is 1.78 Å, while in wurtzite GaN it is 1.95 Å. Bonds in the dislocation core are slightly stretched compared with bulk GaN. The difference in the bond lengths causes an increase in energy for Al atoms when they are close to the dislocation core. This might define the segregation of Al atoms from the dislocation core. This indicates that the electronic structure of the dislocation core is the same as in wurtzite GaN (figure 15) and the screw and threading edge dislocations in AlGaN are electrically inactive. According to our projection of the optimized charge density for certain bands to particular atoms, the occupied N-derived state inside the screw dislocation lies just below the valence-band maximum and the empty Ga-derived state inside the screw dislocation lies above the conduction-band minimum.

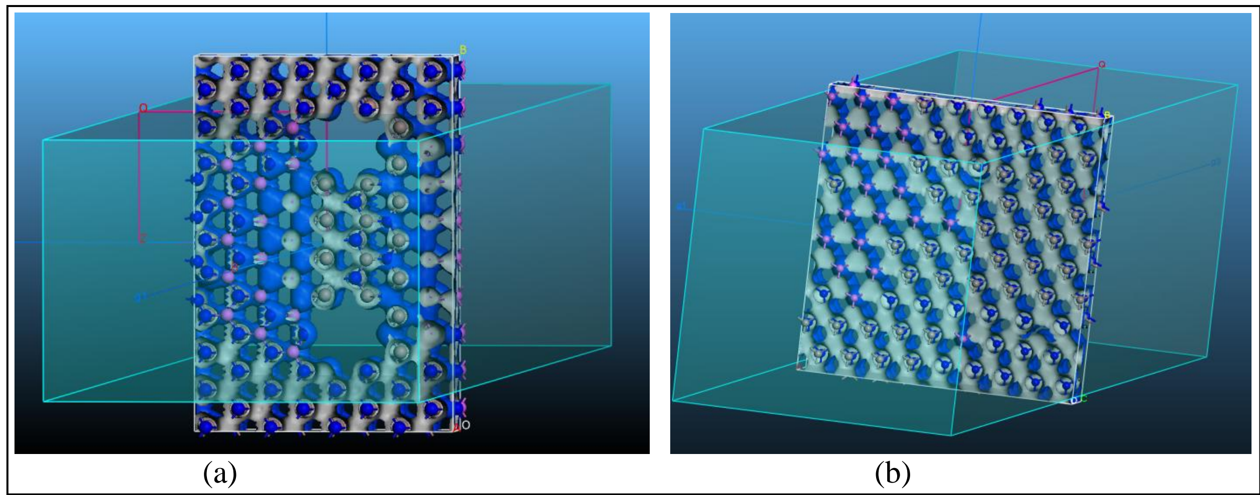

Figure 15. Distribution of Al atoms in (a) screw and (b) edge dislocations in $Al_{0.25}Ga_{0.75}N$ after 10 generations of an evolution with 8 members in each generation. Total charge distribution at isovalue of 0.2 is also shown in the picture. Shadowed region corresponds to Brillouin zone of the supercell.

7. Crystallographic Theory of Dislocations in GaN

7.1 Derivation of Most Probable Slip Systems

The epitaxial growth of a lattice mismatched film begins as an elastically strained pseudomorphic film, and dislocations abruptly form once the thickness exceeds a critical value (*29*). The dislocations usually nucleate at the surface and slip towards the film/substrate interface where they plastically accommodate the mismatch strain (*29, 30*). They can also nucleate internally, but it is unlikely because the activation energy to create one is large (*1, 31*). As is shown in figure 16a (*30*), for growth on the (111) ZB plane one leg of a dislocation loop glides in the $(1\bar{1}\bar{1})$ plane with $\boldsymbol{b} = \frac{1}{2}[\bar{1}0\bar{1}]$, composed of a 60° dislocation with, $\boldsymbol{l} \parallel [\bar{1}\bar{1}0]$; the other leg is a screw dislocation with $\boldsymbol{l} \parallel [\bar{1}0\bar{1}]$.

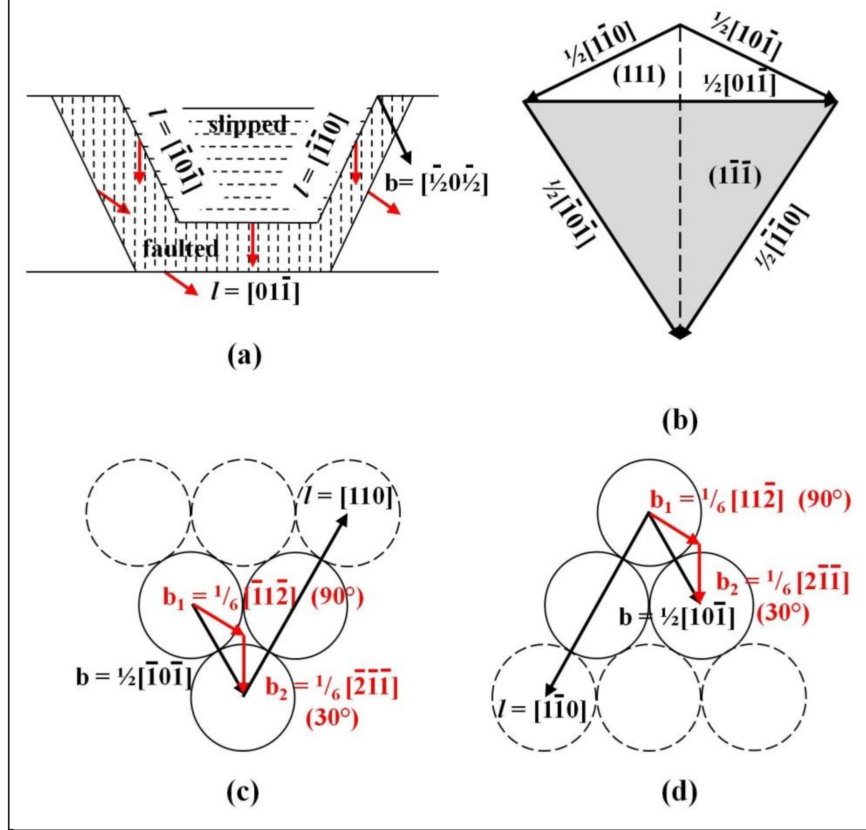

Figure 16. (a) Schematic of a dislocation loop and its associated Burgers vectors, dislocation lines, and partial dislocations for the ZB structure for hetero-epitaxial growth on the (111) plane. (b) The *sp*[3] tetrahedron for the ZB structure with the apex at the origin and the base of the inverted pyramid being parallel to the (111) plane. (c) Atomic packing of the close packed $(1\bar{1}\bar{1})$ ZB plane and the $\frac{1}{2}[\bar{1}0\bar{1}]$ Burgers vector with its associated 60° dislocation line and associated PDs. (d) Atomic packing of the close packed (111) ZB plane, the $\frac{1}{2}[10\bar{1}]$ Burgers vector, with its associated 60° dislocation line and associated PDs.

When the line reaches the interface, $\boldsymbol{l}$ becomes parallel to it and the $[01\bar{1}]$ direction. The Burgers vector can decompose into 90° and 30° partial dislocations separated by a faulted region. (Note that the (111) growth plane is not normal to the paper; rather it makes an angle of 70.5° with it so that the $(1\bar{1}\bar{1})$ slip plane is parallel to the plane of the paper in figure 1.) The *sp*[3] tetrahedron with the apex at the origin, the base of the inverted pyramid parallel to the (111) plane, and the shaded side parallel to the $(1\bar{1}\bar{1})$ slip plane is shown in figure 16b. The partial dislocations (PDs) in the $(1\bar{1}\bar{1})$ slip plane are described in figure 16c with the 90° partial $\boldsymbol{b_1} = \frac{1}{6}[\bar{1}1\bar{2}]$, and the 30° partial $\boldsymbol{b_2} = \frac{1}{6}[\bar{2}\bar{1}\bar{1}]$. The corresponding vectors for the (111) basal plane displayed in figure 16d are $\boldsymbol{b} = \frac{1}{2}[10\bar{1}]$, $\boldsymbol{l}$ (60º) ∥ $[1\bar{1}0]$, $\boldsymbol{b_1} = \frac{1}{6}[11\bar{2}]$, and $\boldsymbol{b_2} = \frac{1}{6}[2\bar{1}\bar{1}]$.

It is equally probable that slip will also occur on the $(\bar{1}\bar{1}1)$ or $(\bar{1}1\bar{1})$ planes because they are identical planes so the shear stress necessary to initiate dislocation flow is the same, but also because the shear stress on these planes generated by the plane strain created by the mismatch

also is the same. For plane strain, the maximum shear stress, τ, occurs on a plane that makes an angle of 45° and it is equal to σ/2, where σ is the longitudinal plane stress, and it is acting in the direction parallel to the intersection of the plane containing the plane normal and the normal to the slip plane. The $(\bar{1}11)$ slip plane and the other two primary slip planes make an angle of 70.6° with the growth plane, which is quite far from the ideal value of 45° so the shear stress on this plane is significantly less than the maximum. In addition, the direction of the shear stress in this plane is the $[\bar{2}\bar{1}\bar{1}]$ direction, which makes an angle of 60° with the slip direction as defined by the direction of a Burgers vector. It is therefore possible that slip could occur on planes other than the primary slip planes in a direction other than the primary slip direction even though it would take more stress to move the atoms because the actual shear stress is much larger on that plane—a plane that makes an angle near 45° with the growth plane and the direction of slip is closer to the direction of the shear stress. These slip systems are called secondary slip systems, which for the most part are not activated in semiconductors with the ZB structure.

For the same tetrahedron referred to the W crystal basis vectors, the vectors in the (0002) basal plane are $\boldsymbol{b} = \frac{1}{3}[2\bar{1}\bar{1}0]$, $\boldsymbol{l}$(60°) ∥ $[1\bar{2}10]$, $\boldsymbol{b_1} = \frac{1}{3}[10\bar{1}0]$, and $\boldsymbol{b_2} = \frac{1}{3}[1\bar{1}00]$. Using the 3-indices notation, the same vectors become $\boldsymbol{b} = [100]$, $\boldsymbol{l}$(60°) ∥ $[0\bar{1}0]$, $\boldsymbol{b_1} = \frac{1}{3}[210]$, and $\boldsymbol{b_2} = \frac{1}{3}[1\bar{1}0]$ (*32*). However, there are no primary slip planes that are active because there is no shear stress in the growth plane, as well as the planes that make an angle of 90° with it. This latter statement eliminates any prismatic plane such as the $(2\bar{1}\bar{1}0)$ or $(10\bar{1}0)$ planes, which are also relatively close packed. The question then is, what is the slip system for hetero-structure W films grown on the (0001) plane?

Slip must occur on a pyramidal plane, and new types of dislocations have to be described. The dislocation with the shortest Burgers vector that lies in a pyramidal plane is, $\boldsymbol{b} = \boldsymbol{c} + \boldsymbol{a} = \frac{1}{3}\langle 11\bar{2}\bar{3}\rangle \rightarrow \langle 11\bar{1}\rangle$, and it is called a mixed dislocation. As shown in figure 17, it can lie in the low index $\{01\bar{1}1\}$, $\{11\bar{2}2\}$, and $\{2\bar{1}\bar{1}1\}$ planes (*33, 34*). This can also be confirmed by the fact that $\boldsymbol{h} \cdot \boldsymbol{b} = 0$, where $\boldsymbol{h}$ is the glide plane represented by three indices created by dropping the *i* index from the $\{hkil\}$ representation. We also briefly consider the next shortest pyramidal Burgers vector, $\boldsymbol{b} = \boldsymbol{c} + 2\boldsymbol{a} = \frac{1}{3}\langle 22\bar{4}3\rangle \rightarrow \langle 22\bar{1}\rangle$, and the associated $\{01\bar{1}2\}$, $\{11\bar{2}4\}$ and $\{2\bar{1}\bar{1}2\}$ slip planes.

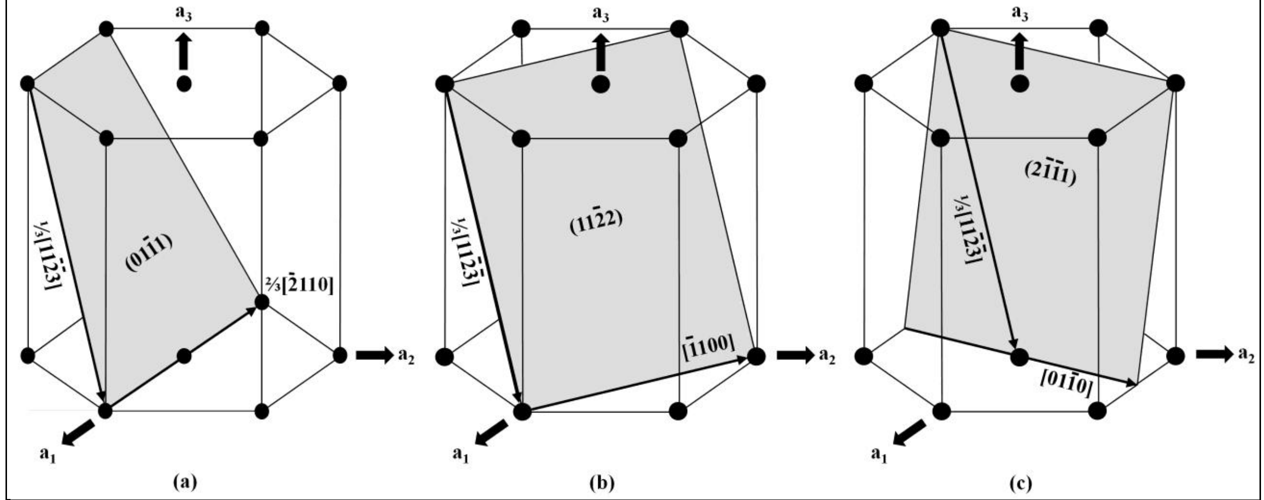

Figure 17. Schematic of the (a) $(01\bar{1}1)$, (b) $(11\bar{2}2)$, and (c) $(2\bar{1}\bar{1}1)$ W planes and the $\frac{1}{3}[11\bar{2}\bar{3}]$ dislocation and associated dislocation line lying in the interfacial (0001) plane.

Slip on these planes is analyzed by determining the angle they make with the (0001) plane, their interplanar spacing, the associated dislocation line, the edge component of the dislocation and the component that lies in the growth plane, and the probable PDs. Then stick models of the bonding structures of planes normal to the glide plane are constructed to examine the cross section of the glide plane and planes parallel to it.

To determine how close **h** approaches this optimum value of making a 45° angle with the (0001) growth plane, the angle (θ) it makes with the basal plane can be determined using the three indices notation from,

$$\cos\theta = \frac{\mathbf{hG}^{-1}(001)}{\left[\mathbf{hG}^{-1}\mathbf{h}\right]^{1/2}\left[(001)\mathbf{G}^{-1}(001)\right]^{1/2}} = \frac{l}{\left[\left(h^2+hk+k^2\right)\left(4\gamma^2/3\right)+l^2\right]^{1/2}} \tag{6}$$

where **G** is the metric tensor for the hexagonal crystal structure, and γ is the *c/a* ratio.

To a first order τ is inversely proportional to the distance between the planes. This distance is the distance between planes with the same Miller indices, *d*, which is found from

$$\frac{1}{d^2} = \mathbf{hG}^{-1}\mathbf{h} = \frac{\frac{4}{3}\left(h^2+hk+k^2\right)+\frac{l^2}{\gamma^2}}{a_H^2} \tag{7}$$

Because there are four atoms associated with the lattice points of the simple hexagonal W unit cell, some planes will have planes with different Miller indices that are parallel to them. For example, the (0002) planes containing only cations are separated by $c/2$, but one plane containing only anions that is parallel to the (0002) plane lies $(½ - u)c$ below it and another is uc above it. To a very good approximation, $u = ⅜$ because $\gamma^2 \approx {}^8/_3$ – the ideal value where all of

the atoms are treated as hard spheres. This value of u is used throughout the report. For some prismatic planes, having four atoms associated with a lattice site is not a problem because the $(2\bar{1}\bar{1}0)$ plane contains all four of them as is illustrated in figure 18. Thus, as seen in figure 18a, stating that the $(2\bar{1}\bar{1}0)$ planes are separated by a distance $a/2$ completely describes all of the atomic sites.

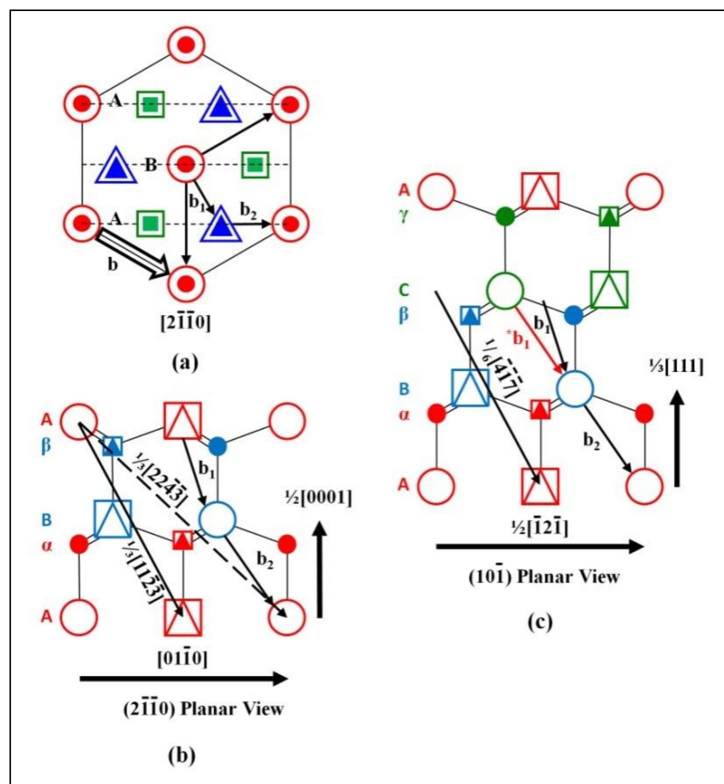

Figure 18. (a) Top (111) planar view and ABA … stacking of the $(10\bar{1})$ ZB planes and the equivalent $(2\bar{1}\bar{1}0)$ W planes. (Cations in ○, ½ or ⅓ above △, and ⅔ above □ the plane; anions ⅜ or ¼ above ●, ⅞ or ½ above ▲, and ¾ above ■.) (b) Side $(2\bar{1}\bar{1}0)$ planar view of the W structure showing the AαBβAα... stacking of the (0002) planes, and (c) side equivalent $(10\bar{1})$ planar view of the ZB structure showing the AαBβCγAα... stacking of the (111) planes. (Cations ○ and anions ● in, cations △ or △, and anions ▲ or ▲ ½ in front of, and cations □ or □ and anions □ or □ ½ behind the plane.)

However, this is not the case when one states that the $(1\bar{1}00)$ W planes are separated by a distance $\sqrt{3}a/2$ because there is also a plane containing atoms $\sqrt{3}a/6$ below it and another one $\sqrt{3}a/3$ above it as is illustrated in figure 19a. Thus, to make certain that all of the atoms are accounted for, it is helpful to use stick figures along with the calculations.

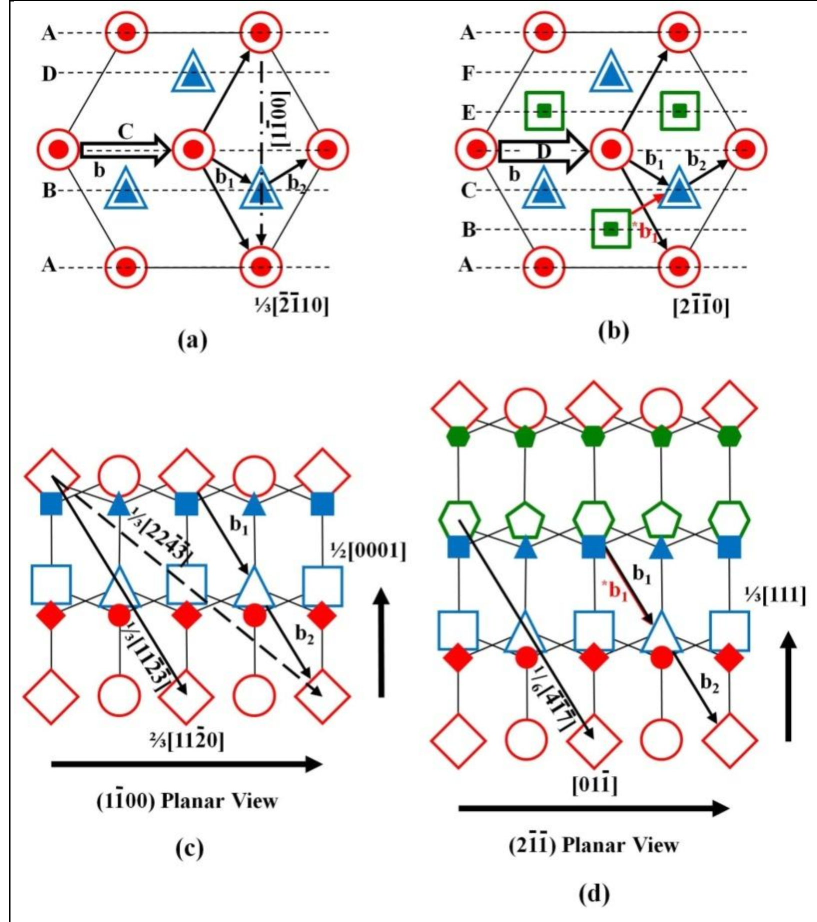

Figure 19. (a) Top (0002) planar view and ABCDA … stacking of the (1$\bar{1}$00) W planes. (b) Side (1$\bar{1}$00) planar view of the W structure showing the AαBβAα... stacking of the (0002) planes. (c) Top (111) planar view and ABCDEF … stacking of the (2$\bar{1}\bar{1}$) ZB planes. (d) Side (2$\bar{1}\bar{1}$) planar view of the ZB structure showing the AαBβCγAα... stacking of the (111) planes. (Cation ○ and anion ● in, cation ⬡ and anion ⬢ $^1/_6$ behind, cation △ and anion ▲ ⅓ behind, cation ◇ and anion ◆ ½ behind, cation ⬠ and anion ⬟ ⅔ behind, and cation □ and anion ■ $^5/_6$ behind the plane.)

The dislocation line, $\boldsymbol{l}$, of **b** when it reaches the interface is parallel to the intersection of the glide and basal planes so that for basal growth plane in the W crystal,

$$\boldsymbol{l} = \mathbf{h} \times (001) = \left[k\bar{h}0 \right] \tag{8}$$

The only component of **b** that contributes to the mismatch is the edge component lying in the growth plane, $b\cos\Phi$, where Φ is the angle between **b** and $\mathbf{b}_G$, the direction normal to the dislocation line and lying in the growth plane. Φ will be the same angle as θ if **b** is an edge dislocation, and therefore normal to $\boldsymbol{l}$. $\mathbf{b}_G$ is given by,

$$\mathbf{b}_G = (001) \times \mathbf{G}\boldsymbol{l} = \left[\left(h + \tfrac{k}{2}\right) \ \left(k + \tfrac{h}{2}\right) \ 0 \right] \tag{9}$$

and $b\cos\Phi$ is determined by the equation,

$$b\cos\Phi = \frac{(\mathbf{bGb})^{1/2}(\mathbf{bGb}_G)}{(\mathbf{bGb})^{1/2}(\mathbf{b}_G\mathbf{Gb}_G)^{1/2}} = \frac{(\mathbf{bGb}_G)}{(\mathbf{b}_G\mathbf{Gb}_G)^{1/2}} \tag{10}$$

For growth on the (0001) plane, equation 10 becomes,

$$b\cos\Phi = \frac{\sqrt{3}}{2}\left[\frac{a_H(hu+kv)}{(h^2+hk+k^2)^{1/2}}\right] \tag{11}$$

where *u, v* and *w* are the indices for **b**.

The Burgers vector can also decompose into partial dislocations, dislocations for which the Burgers vector is not a lattice vector. A necessary condition for decomposition into partials is that $(b_1^2 + b_2^2)/ b^2 = R < 1$, where b_1 and b_2 are the lengths of the partial dislocations, and b is the length of the burgers vector of the dislocation, because the energy is proportional to b^2. The length of the Burgers vector can be calculated using the formula,

$$b^2 = \mathbf{bGb} = \left(u^2 - uv + v^2 + \gamma^2 w^2\right)a_H^2 \tag{12}$$

If partials are formed, they repel each other and in so doing create a stacking fault between them with an energy per unit length, E_γ, that determines the separation distance. Unlike metals where the Burgers vector can be cut into arbitrary lengths to create two PDs (*35, 36*), PDs in covalently bound semiconductors are usually fixed by the separation between two atomic sites for the same type of atom.

The top view in figure 18a represents both the W and ZB structures, the side view in figure 18b is the $(2\bar{1}\bar{1}0)$ planar view of the W structure, and the equivalent $(10\bar{1})$ ZB planar view (*32*) is shown in figure 18c. This planar view was chosen because the $(2\bar{1}\bar{1}0)$ plane is normal to the $(01\bar{1}1)$ plane making it useful for examining cross sections of the $(01\bar{1}1)$ and $(01\bar{1}2)$ planes. Note that both the $(2\bar{1}\bar{1}0)$ W and $(10\bar{1})$ ZB structures have ABA … stacking. The planar view that is useful for examining the cross section of the planes parallel to the $(11\bar{2}2)$ plane is the $(1\bar{1}00)$ W planar view in figure 19b and the corresponding $(2\bar{1}\bar{1})$ ZB planar view in figure 19d. The top views for the structures are shown in figure 19a and 19c, where it is shown that planes parallel to the planar view have ABCDA … stacking in W and ABCDEFA … stacking in ZB. The planar view that is normal to the $(2\bar{1}\bar{1}1)$ plane is the $(01\bar{1}0)$ planar view, but little value is gained from constructing it because the $\frac{1}{3}[11\bar{2}\bar{3}]$ Burgers vector makes a relatively large angle with it, 63.1° when $\gamma^2 = {}^8/_3$.

Choosing the specific W Burgers vector, $\boldsymbol{b} = \frac{1}{3}[11\bar{2}\bar{3}] \rightarrow [11\bar{1}]$, which is equivalent to the $\frac{1}{6}[\bar{4}\bar{1}\bar{7}]$ ZB vector, or $\boldsymbol{b} = \frac{1}{3}[22\bar{4}\bar{3}] \rightarrow [22\bar{1}]$, as well as the stick figures in figures 18 and 19, where the dislocations are represented by thick arrows in the top view, one can assemble table 4.

Table 4. A description of the $\frac{1}{3}[11\bar{2}\bar{3}]$ or $[22\bar{4}\bar{3}]$ dislocations and PDs, and the associated slip planes along with their *d*-spacing and the angle they make with the (0001) growth plane. Where applicable, top is W representation with ZB equivalent below.

b	**h**	***d***	$\boldsymbol{d_{Ideal}}$	$\mathbf{b_1}$	$\mathbf{b_2}$	**R**	$\mathbf{R_{Ideal}}$	***l***	**cosθ**	$\boldsymbol{\theta_{Ideal}}$
$\frac{1}{3}[11\bar{2}\bar{3}]$ $[11\bar{1}]$	$(01\bar{1}1)$ (011)	$\frac{a\gamma\sqrt{3}}{(4\gamma^2+3)^{1/2}}$	0.765a	$\frac{1}{6}[20\bar{2}\bar{3}]$ $\frac{1}{6}[42\bar{3}]$	$\frac{1}{6}[02\bar{2}\bar{3}]$ $\frac{1}{6}[24\bar{3}]$	$\frac{4+3\gamma^2}{6+6\gamma^2}$	0.545	$[2\bar{1}\bar{1}0]$ $[100]$	$\frac{\sqrt{3}}{(3+4\gamma^2)^{1/2}}$	62.1°
$\frac{1}{3}[22\bar{4}\bar{3}]$ $[22\bar{1}]$	$(01\bar{1}2)$ (012)	$\frac{a\gamma\sqrt{3}}{2(\gamma^2+3)^{1/2}}$	0.594a					$[2\bar{1}10]$ $[100]$	$\frac{\sqrt{3}}{(3+\gamma^2)^{1/2}}$	43.3°
$\frac{1}{3}[11\bar{2}\bar{3}]$ $[11\bar{1}]$	$(11\bar{2}2)$ (112)	$\frac{a\gamma}{2(\gamma^2+1)^{1/2}}$	0.426a	$\frac{1}{6}[20\bar{2}\bar{3}]$ $\frac{1}{6}[42\bar{3}]$	$\frac{1}{6}[02\bar{2}\bar{3}]$ $\frac{1}{6}[24\bar{3}]$	$\frac{4+3\gamma^2}{6+6\gamma^2}$	0.545	$[1\bar{1}00]$ $[1\bar{1}0]$	$\frac{1}{(1+\gamma^2)^{1/2}}$	58.5°
$\frac{1}{3}[22\bar{4}\bar{3}]$ $[22\bar{1}]$	$(11\bar{2}4)$ (114)	$\frac{a\gamma}{2(\gamma^2+4)^{1/2}}$	0.316a					$[1\bar{1}00]$ $[1\bar{1}0]$	$\frac{2}{(4+\gamma^2)^{1/2}}$	39.2°
$\frac{1}{3}[11\bar{2}\bar{3}]$ $[11\bar{1}]$	$(2\bar{1}\bar{1}1)$ $(2\bar{1}1)$	$\frac{a\gamma}{(4\gamma^2+1)^{1/2}}$	0.478a					$[0\bar{1}10]$ $[\bar{2}10]$	$\frac{\sqrt{3}}{(1+4\gamma^2)^{1/2}}$	73.0°
$\frac{1}{3}[22\bar{4}\bar{3}]$ $[22\bar{1}]$	$(2\bar{1}\bar{1}2)$ $(2\bar{1}2)$	$\frac{a\gamma}{2(\gamma^2+1)^{1/2}}$	0.426a					$[0\bar{1}10]$ $[\bar{2}10]$	$\frac{1}{(1+\gamma^2)^{1/2}}$	58.5°

Although the $(01\bar{1}1)$ planes have the largest *d*-spacing, they do not have the largest planar density because there are a number of planes containing atoms that are parallel to and lie between them. Assuming that the Ga atom in the lower left hand corner in figure 18b lies at the origin, it can be seen that only the Ga atoms at $[001]$, $[110]$, and $[010]$ lie in the plane. The Ga atoms at $\left[\frac{2}{3}\,\frac{1}{3}\,\frac{1}{2}\right]$ and $\left[-\frac{1}{3}\,\frac{1}{3}\,\frac{1}{2}\right]$ lie in a plane that is a fraction of the *d*-spacing, *f*, above the plane of interest, where

$$f = \frac{\mathbf{u}\cdot\mathbf{n}}{d} - i = \mathbf{u}\cdot\mathbf{h} - i\,, \tag{13}$$

u is the atomic position of an atom in the plane above the plane of interest, **n** is the unit plane normal, and *i* is the number of planes out from the origin that is represented by the trace formed by the intersection of **h** with the planar view. For the $(01\bar{1}1)$ plane in figures 17a and 18b, $i = 1$, and for the $(11\bar{2}2)$ plane in figures 17b and 19b $i = 2$. From equation 12, it can be shown that the Ga atoms at $\left[\frac{2}{3}\,\frac{1}{3}\,\frac{1}{2}\right]$ and $\left[-\frac{1}{3}\,\frac{1}{3}\,\frac{1}{2}\right]$ lie $^{d}/_{6}$ below the $(01\bar{1}1)$ plane ($f = -^{1}/_{6}$). It can also be shown that the N atoms at $\left[-\frac{2}{3}\,\frac{1}{3}\,\frac{7}{8}\right]$ and $\left[-\frac{1}{3}\,\frac{1}{3}\,\frac{7}{8}\right]$ lie in a parallel plane $^{5d}/_{24}$ above the $(01\bar{1}1)$ plane, and the N atoms at $\left[1\;1\;\frac{3}{8}\right]$ and $\left[0\;1\;\frac{3}{8}\right]$ lie in a plane $^{3d}/_{8}$ above it. Thus, instead of a single $(01\bar{1}1)$ plane containing both Ga and N atoms, there is a pair of planes $^{d}/_{6}$ apart containing only Ga atoms, and another pair of planes $^{d}/_{6}$ apart containing only N atoms $^{d}/_{3}$ above the other pair.

Because there are a number of parallel planes containing atoms that lie between the $(01\bar{1}1)$ planes, the atomic planar density, ρ_p, given by,

$$\rho_b = \frac{\rho_a d}{n_p} \tag{14}$$

where $\rho_a = \frac{8}{\sqrt{3}} a_H^2 c$, is the bulk atomic density, and n_p is the number of parallel planes containing atoms between the planes of interest. For the ideal case $\rho_p = 0.541/a_H^2$ for the $(01\bar{1}1)$ plane compared with $1.155/a_H^2$, $1.414/a_H^2$, and $1.225/a_H^2$ for the (0002), $(11\bar{2}0)$ and $(10\bar{1}0)$ planes, respectively.

In addition to having a smaller ρ_p than one would expect when only considering the *d*-spacing, the $[11\bar{2}\bar{3}]$ Burgers vector in the $(01\bar{1}1)$ plane is not a perfect edge dislocation, as it makes an angle of 74.9° with $\boldsymbol{l}$ in the ideal case. This further reduces the probability that the active pyramidal slip system is the $\frac{1}{3}\langle 11\bar{2}\bar{3}\rangle\{01\bar{1}1\}$ slip system. Using equation 11, one calculates that the edge component of the Burgers vector lying in the basal plane is $b\cos\Phi = \frac{1}{2}\sqrt{3}a$. Another negative is that the PDs do not lie in the slip plane. This can be seen in figures 18c and 20b showing the view of the $(01\bar{1}1)$ plane and the atoms in the plane lying above and below it. It can also be confirmed mathematically by the fact that the plane they both lie in, as determined by their cross product, is the $(112) \rightarrow (11\bar{2}2)$ plane.

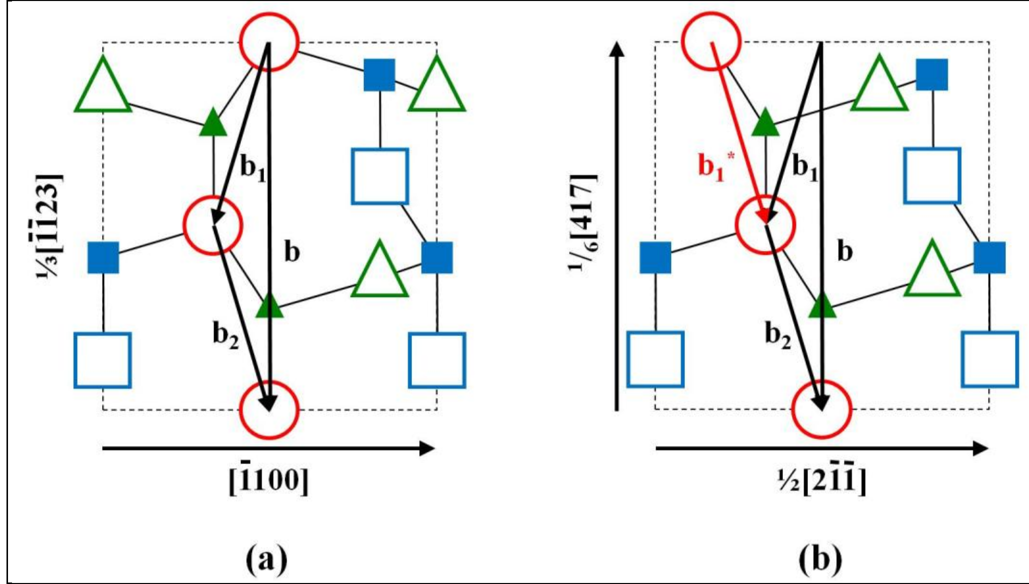

Figure 20. View of the Ga atoms lying in ○, immediately above △, and immediately below □, and the N atoms lying immediately above ▲ and immediately below ■ the (a) $(11\bar{2}2)$ W plane, or (b) $(13\bar{1})$ ZB plane.

Even though the $(01\bar{1}2)$ plane makes an angle close to 45° with the (0002) plane where the maximum shear stress is applied, the greater length of the Burgers vector, the fact that it is not a pure edge dislocation and its effective *d*-spacing is very small make it unlikely that the $\frac{1}{3}\langle 22\bar{4}\bar{3}\rangle\{01\bar{1}2\}$ pyramidal slip system is the active slip system. For the ideal case, $\Phi = 67.2°$ and $\rho_p = 0.420/a^2$. The reason again that it is so low is that there are three planes parallel to the $(01\bar{1}2)$ plane that contain atoms that lie between adjacent $(01\bar{1}2)$ planes. As can be seen in figure 18b, there are two pairs of planes containing either all Ga or all N atoms instead of a single $(01\bar{1}2)$ plane containing both types.

For the $(11\bar{2}2)$ plane shown in figure 17b and its cross section depicted in figure 19b, the planar density is larger than it is for the $(01\bar{1}1)$ plane, even though its *d*-spacing is smaller because only one plane containing atoms, as opposed to three, lie between the $(11\bar{2}2)$ planes. It can be shown that $\rho_p = 0.603/a_H^2$ for the ideal case. Taking the Ga atom in the lower left hand corner of figure 19b to be the origin, the $(11\bar{2}2)$ plane closest to it passes through the Ga atoms at [–⅓ ⅓ ½] and [100]; the trace in figure 19b containing Ga atoms at [001], [⅔ ⅓ ½], and [110] is the second plane out. The single plane containing only N atoms passes through the N atom at $\left[0\ 0\ \frac{3}{8}\right]$, and is $^{d}/_{4}$ below the $(11\bar{2}2)$ plane.

In addition to being the densest plane containing the $\frac{1}{3}[11\bar{2}3]$ dislocation, **b** is a pure edge dislocation, as can be seen in figure 16b, as well as by the fact that $\mathbf{b}\cdot\mathbf{G}\boldsymbol{l} = 0$. As a result, the edge component of the Burgers vector lying in the basal plane is $b\cos\Phi = a_H$, which is larger than it was for the $(01\bar{1}1)$ plane. However, an even stronger argument that the dominant pyramidal slip system for growth on the (0001) plane is the $\frac{1}{3}\langle 11\bar{2}3\rangle(11\bar{2}2)$ slip system is that the likely

partials, $\boldsymbol{b}_1 = \frac{1}{6}[20\bar{2}\bar{3}] \rightarrow \left[\frac{2}{3}\,\frac{1}{3}\,-\frac{1}{2}\right]$ and $\boldsymbol{b}_2 = \frac{1}{6}[02\bar{2}\bar{3}] \rightarrow \left[\frac{1}{3}\,\frac{2}{3}\,-\frac{1}{2}\right]$, lie in the slip plane. This is seen in the stick figure of the $(11\bar{2}2)$ plane in figure 20a showing the structure of the $(11\bar{2}2)$ plane and the planes above and below it, and is confirmed by the fact that $\mathbf{b}_i \cdot \mathbf{h} = 0$. The equivalent Burgers vectors in the ZB structure shown in figure 20b are $[⅔\ ⅓–½]_W \rightarrow {}^1/_6[\underline{114}]_{ZB}$ and $[⅓\ ⅔–½]_W \rightarrow [–½\ 0\ –½]_{ZB}$. Interestingly, $\mathbf{b}_2$ in the ZB structure is a complete dislocation, not a partial, but $\mathbf{b}_1$ is not even a partial as it does not connect atomic sites of similar atoms. This is shown in figure 20b. The reason $\mathbf{b}_2$ is a partial dislocation in the W structure is that the atom at [–⅓ –⅔ ½] in the sp^3 tetrahedron in figure 16b is not at a lattice point, whereas the atom at the equivalent [½ 0 ½] atomic site in the ZB structure is.

The reason that the ${}^1/_6[\overline{114}]_{ZB}$ ZB vector equivalent to the $[⅔\ ⅓–½]_W$ W partial does not connect two atomic sites in the ZB structure is that the third layer in the planar stacking sequence is different in the two structures. However, if the plane with A stacking in the W structure slipped to a C stacking position by a [–⅓ ⅓ 0] slip, the $[⅔\ ⅓–½]_W$ would become $[⅓\ ⅔–½]_W$, which is identical to $\mathbf{b}_2$. This is illustrated in figures 19b and 19d, where the PD, $\mathbf{b}_1$, becomes $\mathbf{b_1}^*$. Combining this Shockley partial with the pyramidal dislocation,

$$\left[1\,1\,\bar{1}\right]+\left[-\frac{1}{3}\;\;\frac{1}{3}\;\;0\right]=\left[\frac{2}{3}\;\;\frac{4}{3}\;\;-1\right]=2\left[\frac{1}{3}\;\;\frac{2}{3}\;\;-\frac{1}{2}\right]_W \rightarrow 2\left[-\frac{1}{2}\;\;0\;\;-\frac{1}{2}\right]_{ZB} \tag{15}$$

This is illustrated in figures 19c, 19d, and 20b. Thus, the $[11\bar{1}]$ pyramidal dislocation not only can readily decompose into two partial dislocations on the $(11\bar{2}2)$ plane, it can, with the additional Shockley partial, decompose into shorter dislocations in the ZB structure. This would stabilize the ZB phase if the reduction in the energy of forming this phase to create shorter dislocations without creating stacking faults is greater than the increase in the energy of formation of this phase. These PDs are Frank partials, which are formed during growth when, e.g., a segment of an Aα double layer is replaced by a Cγ segment or a αB segment is replaced by a γC double layer (*24*). Unlike glissile Shockley dislocations such as those formed by the decomposition of a 60° basal plane dislocation in which the $\mathbf{b_i}$ make an angle of 30° or 90° with $\boldsymbol{l}$, these PDs are sessile and they make angles of $\arccos[\pm 1/(4 + 3\gamma^2)^{½}]$ with $\boldsymbol{l}$.

7.2 Discussion

The transmission electron microscopy (TEM) work of Srinivasan et al. (*33*) on InGaN grown on (0001) GaN, and by Floro et al. (*34*) who grew AlGaN on GaN strongly show that $(\boldsymbol{c} + \boldsymbol{a})$ mismatch dislocations are formed in the film and are not just extensions of dislocations in the substrate. This suggests that the important factor is the magnitude of the strain independent of whether the film is in compression or tension. Further, the latter show that the dislocation lines are parallel to the $\langle 1\bar{1}00\rangle$ directions, and in a GaN film grown on patterned sapphire, they observe dislocations lying in a slip plane making an angle of 59° with the basal plane, which is very close to the 58° computed for the $(11\bar{2}2)$ plane.

There is also strong evidence that the energy of formation for these pyramidal dislocations is high given their long Burgers vector and relatively small interplanar spacing, and that they form only when the slip systems containing the basal and prismatic slip planes are inactive. Liu et al. (*37*) attributed the relatively small reduction in the amount of plastic strain in the growth of InGaN on GaN to the difficulty in forming these dislocations. Also the number of pyramidal dislocations is greatly reduced when growth planes other than the (0001) plane are exposed for growth either by etching the GaN substrate to form etch pits (*38*) or by creating mesas (*39*). This is attributed to basal plane dislocations with smaller critical resolved shear stresses being created instead to relieve the plastic strain now that there are shear stresses on the basal plane.

Given that the plane strain produced by the lattice mismatch during growth on the (0001) plane does not create a shear stress on the basal or prismatic planes, the operational slip plane must be a pyramidal plane. The most probable pyramidal slip system is the $\frac{1}{3}\langle 11\bar{2}\bar{3}\rangle\{11\bar{2}2\}$ slip system. The $\{11\bar{2}2\}$ planes are the most dense pyramidal type plane, there are six different planes so that strain in all directions can be accommodated, and the $(11\bar{2}2)$ plane makes an angle of ~58° with the (0001) plane, which is relatively close to the plane with the maximum shear stress, which is 45°. The Burgers vector is the shortest pyramidal Burgers vector, it is a pure edge dislocation, it can decompose into $\frac{1}{6}\langle 20\bar{2}\bar{3}\rangle$ and $\frac{1}{6}\langle 02\bar{2}\bar{3}\rangle$ Frank PDs that lie in the $\{11\bar{2}2\}$ slip plane, and when a $\frac{1}{3}\langle \bar{1}100\rangle$ partial dislocation is added to it, it can decompose into two identical $\frac{1}{6}[02\bar{2}\bar{3}]$ PDs that correspond to $\frac{1}{2}[\bar{1}0\bar{1}]$ complete dislocations in the ZB structure, which could stabilize this cubic phase.

8. Conclusions

The most important results of this work are the following:

1. Quantum mechanical simulations of threading edge and screw dislocations in AlGaN indicate that Al atoms do not segregate to the dislocation core and atoms in the dislocation core do not produce any defect levels in the bandgap.
2. We performed first time classical MD calculations of dislocation velocity as a function of applied stress for the three slip systems in GaN.
3. The DDD simulator ParaDiS was adapted for calculations of wurtzite semiconductors. Its functionality was demonstrated for hexagonal metals.
4. Based on crystallographic theory we found that given that the plane strain produced by the lattice mismatch during growth on the (0001) plane does not create a shear stress on the basal or prismatic planes, the operational slip plane must be a pyramidal plane. The most probable pyramidal slip system is the $\frac{1}{3}\langle 11\bar{2}\bar{3}\rangle\{11\bar{2}2\}$ slip system. The $\{11\bar{2}2\}$ planes are the most dense pyramidal type plane, there are six different planes so that strain in all

directions can be accommodated, and the $(11\bar{2}2)$ plane makes an angle of ~58° with the (0001) plane, which is relatively close to the plane with the maximum shear stress, which is 45°.

9. References

1. Fitzgerald, E. A.; Xie, Y. H.; Monroe, D.; Silverman, P. J.; Kuo, J. M.; Kortan, A. R.; Thiel, F. A.; Weir, B. E. *J.Vac. Sci. Technol.* **1992**, *B10*, 1807.
2. Queyreau, S.; Marian, J.; Gilbert, M. R.; Wirth, B. D. Edge Dislocation Mobilities in Bcc Fe Obtained by Molecular Dynamics. *Phys. Rev. B* **2011**, *84*, 064106.
3. Plimpton, S. J. Fast Parallel Algorithms for Short-range Molecular Dynamics. *J. Comp. Phys.* **1995**, *117*, 1−19.
4. Nord, J.; Albe, K.; Erhart, P.; Nordlund, K. Modelling of Compound Semiconductors: Analytical Bond-order Potential for Gallium, Nitrogen and Gallium Nitride. *J. Phys.: Condens. Matter* **2003**, *15*, 5649–5662.
5. Brenner, D. Relationship Between the Embedded-atom Method and Tersoff Potentials. *Phys. Rev. Lett.* **1989**, *63* 1022.
6. Harafuji, K.; Tsuchiya, T.; Kawamura, L. Molecular Dynamics Simulation of Dislocations in Wurtzite-type GaN Crystal. *J. Appl. Phys.* **2004**, *96*, 2513–2524.
7. Rodney, D. Activation Enthalpy for Kink-pair Nucleation of Dislocations: Comparison Between Static and Dynamic Atomic-scale Simulations. *Phys. Rev. B* **2007**, *76*, 144108.
8. Li, J. AtomEye: An Efficient Atomistic Configuration Viewer. *Modelling Simul. Mater. Sci. Eng.* **2003**, *11*, 173.
9. Arsenlis, A.; Cai, W.; Tang, M.; Rhee, M.; Oppelstrup, T.; Hommes, G.; Pierce, T. G.; Bulatov, V. V. *Modelling Simul. Mater. Sci. Eng* **2007**, *15*, 553.
10. Wu, C.-C.; Aubry, S.; Chung, P. W.; Arsenlis, A. *Mater. Res. Soc. Symp. Proc.* **2012**, *1424*.
11. Damiano V. V. *Trans. Metall. Soc. AIME* **1963**, *227*, 788.
12. Martinez, E.; Marian, J.; Arsenlis, A.; Victoria, M.; Perlado, J. M. *J. Mech. Phys. Sol.* **2008**, *6*, 869.
13. Yoo, M. H.; Agnew, S. R.; Morris, J. R.; Ho, K. M. *Mater. Sci. Eng. A* **2001**, *319–321*, 87.
14. deWit, G.; Koehler, J. S. *Phys. Rev.* **1959**, *116*, 1113.
15. Frank, F. C.; Read, W. T. *Phys. Rev.* **1950**, *79*, 722.
16. Dash, W. C. *J. Appl. Phys.* **1956**, *27*, 1193.
17. Dupuy, L.; Fivel, M. C. *Acta Materialia* **2002**, *50*, 4873.

18. Shenoy, V. B.; Kukta, R. V.; Phillips, R. *Phys. Rev. Lett.* **2000**, *84*, 1491.

19. Hull, D.; Bacon, D. J. *Introduction to Dislocations*; (Elsevier, 2001).

20. Capolungo L. *Acta Materialia* **2011**, *59*, 2909.

21. Rodney, D.; Phillips, R. *Phys. Rev. Lett.* **1999**, *82*, 1704.

22. Shenoy, V. B.; Kukta, R. V.; Phillips, R. *Phys. Rev. Lett.* **2000**, *84*, 1491.

23. Osipiyan, Y. A.; Smirnova, I. S. *Phys. Stat. Sol.* **1968**, *30*, 19.

24. Osipiyan, Y. A.; Smirnova, I. S. *J. Phys. Chem. Solids* **1971**, *32*, 1521.

25. Batyrev, I. G.; Sarney, W. L.; Nguyen, C.; Rice, B. M.; Jones, K. A. *Phys. Stat. Sol. (A)* **2011**, *208*, 1566.

26. Wu, F.; Lin, Y. D.; Chakraborty, A.; Ohta, H.; DenBaars, S. P.; Nakamura, S.; Speck, J. S. *Appl. Phys. Lett.* **2010**, *96*, 231912.

27. Oganov A. R.; Glass C. W. Crystal Structure Prediction using *Ab Initio* Evolutionary Techniques: Principles and Applications. *J. Chem. Phys.* **2006***, 124,* art. 244704.

28. Kresse G.; Furthmüller J. Efficient Iterative Schemes for *Ab Initio* Total-energy Calculations Using a Plane Wave Basis Set. *Phys. Rev. B* **1996**, *54*, 11169–11186.

29. Matthews, J. W.; Blakeslee, A. E. *J. Crystal Growth* **1974**, *27*, 118.

30. te Nijenhuis, J.; van der Wei, P. J.; van Eck, E.R.H.; Giling, L. J. *J. Phys. D* **1996**, *29*, 2961.

31. Matthews, J. W.; Blakeslee, A. E.; Moder, S. *Thin Sol. Films* **1976**, *33*, 253.

32. Jones, K. A. *J. Crystal Growth* **2008**, *310*, 2417.

33. Srinivasan, S.; Geng, L.; Liu, R.; Ponce, F. A.; Narukawa, Y.; Tanaka, S. *Appl. Phys. Lett.* **2003**, *83*, 5187.

34. Floro, J. A.; Follstaedt, D. M.; Provercio, P.; Hearne, S. J.; Lee, S. R. *J. Appl. Phys.* **2004**, *96*, 7087.

35. Numakura, H.; Koiwa, M. *Metall. Sci. Technol.* **1998**, *16*, 4–19.

36. Yoo, H. H.; Morris, J. R.; Ho, K. M.; Agnew, S. R. *Metall. & Mat. Trans.* **2002**, *33A*, 813.

37. Sato, H.; Chung, R. B.; Hirasawa, H.; Fellows, N.; Masui, H.; Wu, F.; Saito, M.; Fujito, K.; Speck, J. S.; DenBaars, S. P.; Nakamura, S. *Appl. Phys. Lett.* **2008**, *92*, 221110.

38. Liu, R.; Mei, J.; Srinivasan, S.; Omiya, H.; Ponce, F. A.; Cherns, D.; Narakawa, Y.; Mukai, T. *Jpn. J.Appl. Phys., Part 2* **2006**, *45*, L549.

39. Liu, R.; Mei, J.; Srinivasan, S.; Ponce, F. A.; Omiya, H.; Narukawa, Y.; Muka, T. *Appl. Phys. Lett.* **2006**, *89*, 201911.

10. Transitions

Results of the report will be used in Sensors and Electron Devices Directorate (SEDD) efforts to grow AlGaN on AlN. The Army Research Office (ARO) has a Small Business Technology Transfer Program (STTR) to experimentally look at how one can grow AlGaN on either GaN or AlN substrates and confine the dislocations to near the interface so that the material near the surface has fewer dislocations to interfere with the lateral devices built on it. K. A. Jones organizes a workshop on January 31, 2013 to discuss the STTR work and most important results of the DRI report. Results of the report will be also used in a pending approval I3M project on dislocation dynamics in GaN, Be, and Mg (principal investigator [PI] P. W. Chung).

List of Symbols, Abbreviations, and Acronyms

2DEG	two-dimensional electron gas
Al	aluminum
AlGaN	aluminum gallium nitride
AlN	aluminum nitride
Be	beryllium
cpp	close packed plane
DDD	discrete dislocation dynamics
DFT	density functional theory
DoD	Department of Defense
fcc	face centered cubic
Ga	gallium
GaAs	gallium arsenide
GaN	gallium nitride
Ge	germanium
hcp	hexagonal close packed
HEMTs	high electron mobility transistors
HPICs	high power integrated circuits
ICs	integrated circuits
InGaN	indium gallium nitride
LAMMPS	Large-Scale Atomic/Molecular Massively Parallel Simulator
MD	molecular dynamics
Mg	magnesium
N	nitrogen
PD	partial dislocation

RF	radio frequency
Si	silicon
SiC	silicon carbide
SiGe	silicon germanium
TEM	transmission electron microscopy
UV	ultraviolet
VASP	Vienna Ab-Initio Simulation Package
W	wurtzite
ZB	zincblende

NO. OF COPIES	ORGANIZATION
18 HCS	US ARMY RSRCH LAB RDRL WMB B I BATYREV (2 CPS) N S WEINGARTEN (2 CPS) B RICE N TRAVERDI RDRL CIH C C-C WU (2 CPS) P CHUNG J CLARKE R NAMBURU J KNAP J CRONE L MUNDAY RDRL WMP B M GEENFIELD J CLAYTON RDRL WMM B G GAZONAS RDRL WM J MCCAULEY 4600 DEERCREEK LOOP APG MD 21005-5069
6 HCS	US ARMY RSRCH LAB RDRL SED E K A JONES (2CPS) T ZHELEVA RDRL SEE I W SARNEY RDRL SEE M M WRABACK M REED 2800 POWDER MILL RD ADELPHI MD 20783-1197
1 (PDF only)	DEFENSE TECHNICAL INFORMATION CTR DTIC OCA 8725 JOHN J KINGMAN RD STE 0944 FORT BELVOIR VA 22060-6218

NO. OF COPIES	ORGANIZATION
1 HC	DIRECTOR US ARMY RESEARCH LAB IMAL HRA 2800 POWDER MILL RD ADELPHI MD 20783-1197
1 HC	DIRECTOR US ARMY RESEARCH LAB RDRL CIO LL 2800 POWDER MILL RD ADELPHI MD 20783-1197
1 HC	ADROIT MATERIALS ZLATKO SITAR 3001 GREYHAWK PL APEX NC 27539
1 HC	KYMA TECHNOLOGIES KEITH EVANS 8829 MIDWAY WEST RD RALEIGH NC 27617
1 HC	UNIVERSITY AT ALBANY-SUNY F (SHADI) SHAHEDIPOUR-SANDVIK 257 FULLER ROAD ALBANY NY 12203
1 HC	US ARMY RESEARCH OFFICE RDRL ROE M CHAKRAPANI VARANASI PO BOX 12211 RESEARCH TRIANGLE PARK NC 27709-2211
1 HC	JOHNS HOPKINS UNIV DEPT OF MECH ENGRNG KT RAMESH 3400 CHARLES ST BALTOMIRE MD 21218
2 HCs	DIR USARL US ARMY RSRCH LAB RDRL D O OCHOA T ROSENBERGER 2800 POWDER MILL RD ADELPHI MD 20783-1197